

cb

Deterministic and Stochastic Modeling of the Water Entry and Descent of Three-Dimensional Cylindrical Bodies

by

Jennifer L Mann

B.S., Ocean Engineering (2002)
Florida Atlantic University

Submitted to the Department of Ocean Engineering
in partial fulfillment of the requirements for the degree of

Master of Science in Ocean Engineering

at the


MASSACHUSETTS INSTITUTE OF TECHNOLOGY

June 2005

© 2005 Massachusetts Institute of Technology

All Rights Reserved

Author.....

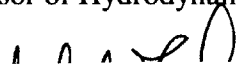


Department of Ocean Engineering
May 6, 2005

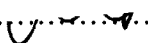
Certified By.....



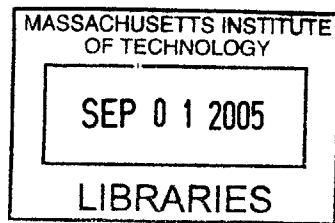
Dick K.P. Yue
Professor of Hydrodynamics and Ocean Engineering
Thesis Supervisor



Accepted By.....



Michael S. Triantafyllou
Chair, Departmental Committee on Graduate Students



BARKER

Deterministic and Stochastic Modeling of the Water Entry and Descent of Three-Dimensional Cylindrical Bodies

by

Jennifer L Mann

Submitted to the Department of Ocean Engineering
on May 6, 2005 in partial fulfillment of the
requirements for the degree of
Master of Science in Ocean Engineering

Abstract

An effective physics-based model has been developed that is capable of reliably predicting the motion of a three-dimensional mine-shaped object impacting the water surface from air and subsequently dropping through the water toward the sea bottom. This deterministic model, MINE6D, accounts for six-degree-of-freedom motions of the body. MINE6D allows for physics-based modeling of hydrodynamic effects due to water impact, viscous drag associated with flow separation and vortex shedding, air entrainment, and realistic flow environments. Unlike existing tools that are limited to plane motions only, MINE6D captures the myriad of complex three-dimensional motions of cylindrical mines observed in field and laboratory experiments.

In particular, accounting for the three-dimensional viscous drag and air entrainment cavity produces an accurate prediction of the velocity, trajectory, and orientation of mines freely dropping in the water. The model development and effects on body motion are presented for both viscous drag and air entrainment cavities. Monte Carlo simulation using MINE6D is then used to obtain statistical characterization of mine motions in practical environments. These statistical results are not only the essential input for stochastic bottom impact and burial predictions of mines but also important for the design of mines.

Thesis Supervisor: Dick K.P. Yue

Title: Professor of Hydrodynamics and Ocean Engineering

Acknowledgements

This could not have been possible without the love and support of my mom, Amy Mann.

The Office of Naval Research under the Mine Burial Predication Program, Grant N00014-01-1-0336, financially supported this research.

Contents

Abstract.....	2
Acknowledgements.....	3
List of Figures.....	6
List of Tables.....	9
Chapter 1.....	10
1.1 Motivation.....	10
1.2 Water-Entry and Descent.....	11
1.3 Physics – Based Simulation Model.....	12
Chapter 2.....	13
2.1 Equations of Motion.....	13
2.2 Modeling Of Physical Processes.....	15
2.3 Structure of MINE6D.....	16
2.4 Predictive Capability of MINE6D.....	18
2.4.1 Straight Motion.....	18
2.4.2 Straight-Slant Motion.....	18
2.4.3 Nose Turn Motion.....	18
2.4.4 See-Saw Motion.....	20
2.4.5 Tumbling Motion.....	20
2.4.6 Travel Motion.....	20
2.4.7 Spiral.....	20
2.4.8 Combined.....	20
Chapter 3.....	21
3.1 Computation of Viscous Drag on a Slender Cylindrical Mine.....	21
3.1.1 Finite length cylinders in normal flow.....	21
3.1.2 Finite length cylinder in oblique flow.....	22
3.1.3 Sensitivity of mine motions to drag modeling.....	24
3.2 Water Impact of Mines Dropping from the Air.....	30
3.3 Air Entrainment Cavity Model.....	31
3.3.1 Types of Air Entrainment Cavities.....	31
3.3.2 Air Cavity Formation and Model.....	33
3.3.3 Bubble After Cavity Closure.....	38
3.3.4 Modeling of air entrainment in MINE6D.....	40
3.4 Environmental Conditions.....	44

Chapter 4.....	46
4.1 Monte Carlo Simulation.....	46
4.2 Statistical Characterizations.....	49
4.2.1 Characterizations of Different Drag Coefficients	49
4.2.2 Characterizations of Different Aspect Ratios	55
4.3 Design Applications.....	62
Chapter 5.....	65
5.1 Summary	65
5.2 Future Work.....	65
Bibliography	67
Appendix A : Sample Program Input.....	71
Appendix B: Drag Treatment Detailed Mine Models.....	72
Appendix C: Design Application Detailed Mine Models.....	73
Appendix D: Aspect Ratio Detailed Mine Models.....	77

List of Figures

Figure 2.1 Global coordinate system (X, Y, Z) and locale coordinate system (x, y, z)....	13
Figure 2.2 MINE6D Flowchart of Physic Modeling	17
Figure 2.4 Trajectories of the mine predicted by MINE6D for (a) see-saw motion and (b) spiral motion.....	19
Figure 3.1: Span wise drag coefficient profiles used in MINE6D as given by equations 3.1 and 3.2. The profile used can be user specified.	24
Figure 3.2 Comparison of the effect of drag coefficient treatment on resulting motion. a) A uniform drag coefficient profile is used. b) Cubic drag coefficient profile is used. The cubic drag coefficient has an asymmetric profile that is appropriate for the release angle.....	27
Figure. 3.3 Total Velocity VS Depth for the trajectories shown in figure 3.2.....	27
Figure 3.4 Comparison of the effect of drag coefficient treatment on resulting motion a) A uniform drag coefficient profile is used. b) A cosine drag coefficient profile is used. The cosine profile causes the mine to descend more quickly.....	28
Figure 3.5 Total Velocity VS Depth for the trajectories shown in figure 3.4.....	28
Figure 3.6 Comparison of the effect of drag coefficient treatment on resulting motion. a) A linear drag coefficient profile is used. b) A cosine drag coefficient is used. The different drag treatments do not cause appreciable alterations to the trajectory or velocity.....	29
Figure 3.7 Total Velocity VS Depth for the trajectories shown in figure 3.6.....	29
Figure 3.8: Impact of mine with the free surface. The highlighted section in red shows the change in the submerged portion of the body through impact.....	31
Figure 3.9 The parameters used to describe the cavity formation and pinch off. D is the cylinder diameter. H is the total depth of the cavity to ½ of the top of the cylinder. z _c is depth from the surface where the cavity pinches off. h _c is the height from the pinch off of the cavity to the ½ top of the cylinder. V _i is the velocity of the cylinder downwards. u is the velocity of the cavity wall inward to the middle.....	33
Figure 3.10: Comparison of air cavity model to disk experiments conducted by Glasheen and McMahon [6] for low Froude numbers. α = 1.45	37

Figure 3.11 On the left is the bubble after pinch off. On the right is the equivalent volume spherical volume.	38
Figure 3.12 Comparison of the acceleration with the cavity and an experiment from NGLI Site 9, Drop 8 [17]. The cavity model shows the dramatic deceleration while the cavity is present.....	42
Figure 3.13 Visualization of the comparison of the cavity model (red) and non-cavity model (light blue). The cavity model descends more slowly and has less translational motion.	42
Figure 3.14 Acceleration of mine with air entrainment, comparison of acceleration for a field experiment (NGLI Site 9, Drop 8B) with an air cavity is formed from the drop to MINE6D with the air cavity and bubble model ($\beta = 13$) and to MINE6D without air cavity consideration. The cavity is open to air between 0 and .425 seconds. The cavity closes and a bubble follows the mine from 0.425 seconds and 0.8 seconds.	43
Figure 3.15 Acceleration with MINE6D bubble model for differing decay rates, $\beta = 5, 13,$ and 25. The time shown is from cavity closure forward. The higher the β value is, the faster the decay of the bubble. β needs to be calibrated against experimental results.....	44
Figure 3.16 Environmental Effects a) Current Profile Used in MINE6D b) From Abelev[1] Presence of current in field test in LA c) Presence of current in MINE6D....	45
Figure 4.1 Histogram and Guassian PDF of the initial horizontal velocity. The specified μ_x is 0.5 m/s and σ_x is 0.25. The scaled Guassian PDF for the specified mean and standard deviation plotted over a histogram of 800 random variables created for the Monte Carlo Simulation.....	48
Figure 4.2 Histogram and Guassian PDF of the initial angle. The specified μ_y is 45 degrees and σ_y is 30 degrees. The scaled Guassian PDF for the specified mean and standard deviation plotted over a histogram of 800 random variables created for the Monte Carlo Simulation.....	48
Figure 4.3 Bottom velocity histogram for uniform drag treatment for 200 simulations ..	51
Figure 4.4 Bottom velocity histogram for cosine drag treatment for 200 simulations	51
Figure 4.5 Bottom velocity histogram for linear drag treatment for 200 simulations	52
Figure 4.6 Bottom velocity histogram for cubic drag treatment for 200 simulations.....	52
Figure 4.7 Bottom pitch angle histogram for uniform drag treatment for 200 simulations	53

Figure 4.8 Bottom pitch angle histogram for cosine drag treatment for 200 simulations	53
Figure 4.9 Bottom pitch angle histogram for linear drag treatment for 200 simulations .	54
Figure 4.10 Bottom pitch angle histogram for cubic drag treatment for 200 simulations	54
Figure 4.11 The drag coefficient profile over the normalized length of the cylinder as evaluated by equation 3.1 for different aspect ratios	57
Figure 4.12 Bottom velocity histogram for aspect ratio of 2.0 for 200 simulations.....	58
Figure 4.13 Bottom velocity histogram for aspect ratio of 4.5 for 200 simulations.....	58
Figure 4.14 Bottom velocity histogram for aspect ratio of 7.0 for 200 simulations.....	59
Figure 4.15 Bottom velocity histogram for aspect ratio of 9.5 for 200 simulations.....	59
Figure 4.16 Bottom pitch angle histogram for aspect ratio of 2.0 for 200 simulations....	60
Figure 4.17 Bottom pitch angle histogram for aspect ratio of 4.5 for 200 simulations....	60
Figure 4.18 Bottom pitch angle histogram for aspect ratio of 7.0 for 200 simulations....	61
Figure 4.19 Bottom pitch angle histogram for aspect ratio of 9.5 for 200 simulations....	61
Figure 4.20 Plot of Final Velocity Vs Initial Release Angle For Sample Mine Types	63
Figure 4.21 Plot of Final Pitch Vs Initial Release Angle For Sample Mine Types.....	64

List of Tables

Table 3.1 Regimes of Cavity Formation Based on the Froude Number.....	32
Table 3.2 Comparison of experimental results with the prediction used in equation 3.10 for a given initial velocity	36
Table 3.3 Compares measured bubble oscillations from NGLI Site Experiments and the predicted bubble oscillation from equation 3.11. The measured time of the cavity closure was used to determine the radius of the bubble for the predicted value.	40
Table 4.1 Bottom velocity and bottom pitch angle means and standard deviations for different drag treatments.	55
Table 4.2 Mine properties for different aspect ratios. The mine dimensions were chosen that all mines being evaluated would have the same volume and weight	57
Table 4.3 Bottom velocity and bottom pitch angle means and standard deviations for different aspect ratios.	62
Table 4.4 Sample of Mine Characteristics Tested	62

Chapter 1

Introduction

1.1 Motivation

Underwater mines are an increasing threat to the US Navy Fleet. Relatively inexpensive mines can cause massive damage to a vessel and possible death to her passengers. Proper modeling of the hydrodynamics of a body impacting the water surface and then falling through the water is essential to the success of mine burial predictions, as it provides the necessary input on the motion of the body to the mine penetration models. Reliable prediction of mine burial is of practical importance to the mine deployment and mine countermeasures in Navy operations. Current mine detection methods need to be enhanced with more sophisticated prediction tools.

The existing tool, IMPACT 25/28, accounts for the plane motion of a mine only [29], and does not model the dynamics of rotational motion of the body. Thus, IMPACT 25/28 cannot capture the complex three-dimensional motions observed in field and laboratory experiments [17, 22]. In particular, IMPACT 25/28 usually over predicts the velocity of the mine and gives incorrect prediction of the orientation of the mine as the mine approaches to impact the bottom [17].

Recent field and laboratory experiments show that even cylindrical mines exhibit a myriad of complex three-dimensional motions depending on the releasing condition, flow environments, and mass properties of the mine [1, 21]. Accurate prediction of the trajectory, velocity, and orientation of a mine falling from air and subsequently dropping in the water toward the sea bottom is an extremely challenging task. Both the six-degree-of-freedom rigid body dynamics including hydrodynamic interactions must be considered and the physical effects due to water surface impact, flow separation and vortex shedding, air entrainment, and ambient flow environments need to be properly accounted.

1.2 Water-Entry and Descent

In water entry from the air, a mine experiences impact with the water's surface and large drag due to an air entrainment behind the mine. Most existing studies on water impact are for two-dimensional bodies and based on a flat (von Karman's method) or near-flat (Wagner's approach) free surface [24]. Recently, a generalized Wagner approach [13], based on the extension of the Wagner's asymptotic theory to arbitrary body geometry and entry angle, has been developed and shown to be quite effective for two-dimensional bodies. The similar effectiveness of such a semi-analytic approach for general three-dimensional bodies is expected. After the impact with the water surface, an air entrainment may be formed behind the mine. Based on the experimental study of water entry of a circular disk at low Froude numbers, [4,6] developed a simple model for the computation of the drag on the disk due to the entrained air. Lee et al [9] developed a more complex numerical model for very high Froude numbers that considers the motion of the projectile and the nonlinear evolution of the free surface. However since the majority of mine drops occur at relatively low Froude numbers, the model of [4,6] is more appropriate to this application.

The motion of a three-dimensional bluff body in the water is significantly affected by viscous drag associated with flow separation and vortex shedding [11,16, 23]. Though extensive literature exists for viscous flow around two-dimensional bodies, there are far fewer studies on viscous flow around three-dimensional bodies. Even for a finite length slender cylindrical mine, fluid flows around ends of the body are strongly three-dimensional that makes it difficult to compute the viscous drag on the body accurately [15]. When the cylinder is placed normal to the flow, the finite length of the body creates a larger localized drag coefficient near the ends due to the creation of vortices from flow around the ends [23]. Overall, the drag on a finite length cylinder is generally less than that obtained based on the strip theory with the drag coefficient of the two-dimensional cylinder [19, 23]. The situation is much more complicated when the cylinder is yawed (or orientated at some angle to the flow) [20]. Again the drag coefficient at the ends differs from that in the midsection of the body. The exact distribution of the drag along the body depends on the Reynolds number, yaw angle, and aspect ratio of the body [8].

The environmental forcing due to ambient current and surface waves also plays an important role [1] in the drop motion of the mine. Waves and current can affect the motion of the mine by inducing an excitation and/or extra viscous drag on the body. Though the exact environmental conditions are hard to measure during mine deployment, the inclusion of environmental forcing is important to the understanding of the basic dynamics of mine drop motion

1.3 Physics – Based Simulation Model

This thesis presents an effective deterministic model, MINE6D, for reliably predicting the motion of a cylindrical mine impacting the water surface from air and dropping in the water. This model considers the six-degree-of-freedom motion of the body including relevant hydrodynamic effects. In particular, the virtual mass matrix is computed exactly using the boundary integral equation method. MINE6D captures the key features of complex motions observed in the field and laboratory dropping tests [1, 21, 22] and offers substantial improvements over IMPACT 25/28. MINE6D allows physics-based drag modeling improvement to capture the complexities of three-dimensional flow around a finite length cylindrical mine. To further the accuracy of predictions, MINE6D employs the physics-based models to account for the physical effects associated with water-entry impact, air entrainment, and environmental forcing due to current and surface waves.

Finally, this deterministic model is used in a Monte Carlo simulation to obtain stochastic characterizations of mine motion in the water and to provide the necessary stochastic input of mine orientation and kinematics (near the bottom) for statistical mine burial predictions.

Chapter 2

Model Development

2.1 Equations of Motion

The general problem of a three-dimensional body released in the air above the water surface and then freely falling through the water is considered for predicting the drop motion of mines. To describe the six degree-of-freedom motion of the body, two coordinate systems are defined: one is the space-fixed inertia (global) coordinate system (XYZ), and the other is the body-fixed (local) coordinate system (xyz) with the origin located at the center of mass of the body and the x-axis pointing in the longitudinal direction of the body, as shown in figure 2.1.

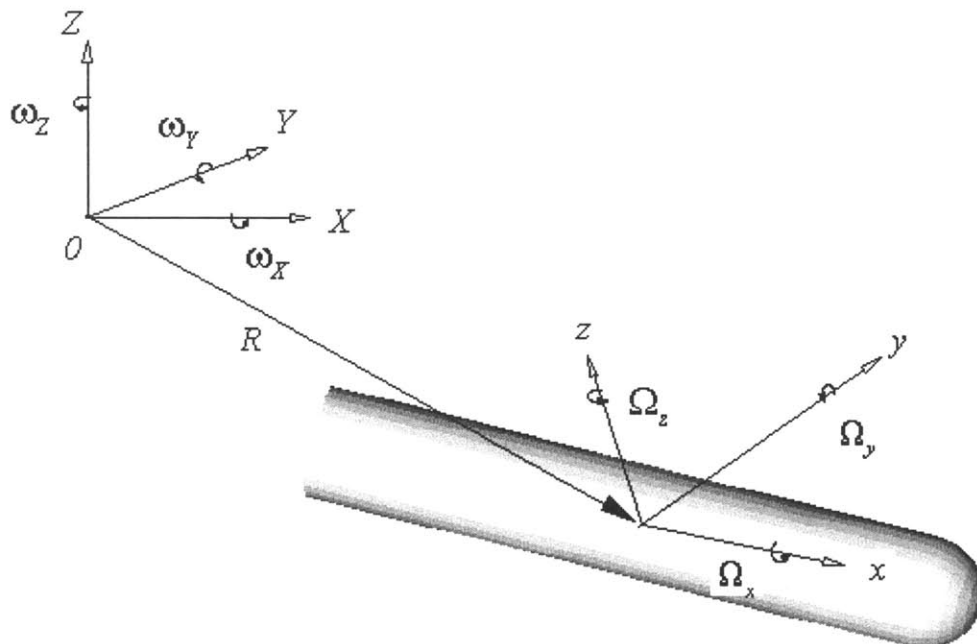


Figure 2.1 Global coordinate system (X, Y, Z) and locale coordinate system (x, y, z) from [28].

In the global coordinate system, the equations of motion of the body may be expressed as

$$\begin{aligned}\bar{F}_o = m & \left(\frac{d}{dt} \bar{v}_o - \bar{v}_o \times \bar{\omega} - (\bar{\omega} \times \bar{R}) \times \bar{\omega} - \bar{R} \times \frac{d}{dt} \bar{\omega} \right) \\ & + [m_A]_{11} \frac{d}{dt} \{\bar{v}_o\} + [m_A]_{12} \frac{d}{dt} \{\bar{\omega}\} + \{\bar{v}_o\} \frac{d}{dt} [m_A]_{11} + \{\bar{\omega}\} \frac{d}{dt} [m_A]_{12}\end{aligned}\quad [2.1]$$

$$\begin{aligned}\bar{M}_o = [L]^T & \left([I'] \frac{d}{dt} \{\bar{\Omega}\} + \{\bar{\Omega}\} \times ([I'] \{\bar{\Omega}\}) \right) \\ & + m \left(\bar{R} \times \frac{d}{dt} \bar{v}_o + (\bar{v}_o \times \bar{\omega}) \times \bar{R} + (\bar{R} \times \frac{d}{dt} \bar{\omega}) \times \bar{R} \right) \\ & + [m_A]_{21} \frac{d}{dt} \{\bar{v}_o\} + [m_A]_{22} \frac{d}{dt} \{\bar{\omega}\} + \{\bar{v}_o\} \frac{d}{dt} [m_A]_{21} \\ & + \{\bar{\omega}\} \frac{d}{dt} [m_A]_{22}\end{aligned}\quad [2.2]$$

\bar{F}_o and \bar{M}_o are the external force and moment on the body due to gravity, buoyancy, viscous effects and environmental forcing, \bar{v}_o and $\bar{\omega}$ are the translational and rotational velocities of the local coordinate system with respect to the global coordinate system, $\bar{\Omega}$ is the angular velocity of the body with respect to the local coordinate system, \bar{R} is the displacement vector of the origin of the local system, m is the mass of the body, $[I']$ is the moment matrix of the body mass with respect to the local axes, $[m_A]_{ij}$ represents the sub-matrix of the added-inertia matrix, and $[L]$ is the transformation matrix between the global frame and the local frame in terms of the Euler angles [28].

The velocity, orientation, attitude of the body during the drop of a mine can be determined by solving the above equations of motion. This is achieved by numerically integrating these coupled ordinary differential equations with time starting with specified initial conditions. In MINE6D, the 4-th order Runge-Kutta integration method is employed. At each time, it is necessary to accurately evaluate the added-inertia matrix, $[m_A]$ of the body. The boundary value problem in the potential flow formulation is solved numerically by the boundary integral equation method. To avoid continuously solving the

boundary value problem at each time step of the simulation, the added-inertia matrix in the local frame is utilized. The transformation matrix is used to convert the added-inertia matrix in the local frame to that in the global frame

2.2 Modeling Of Physical Processes

For a freely falling body, the external force and moment contain components due to gravity, buoyancy, viscous effects, and environmental forcing associated with ambient current and surface waves. Among these, accurate evaluation of viscous effects and environmental forcing is challenging. In particular, due to the lack of understanding of the complex dynamic processes associated with flow separation and vortex shedding around a three-dimensional body, an accurate account of the viscous effect is difficult. The MINE6D model uses a relatively simple quasi-steady approach for the evaluation of the viscous force/moment on the body. In this approach, the viscous force on the body, in the body-fixed (i.e. local) frame, is evaluated by

$$\{\bar{F}_V\} = \left\{ \begin{array}{l} \frac{1}{2} \rho C_{D,x=\pm L/2} S_x |v_x| v_x \\ \frac{1}{2} \rho \int C_{D,YZ}(x) S(x) |v_y(x)| v_y(x) dx \\ \frac{1}{2} \rho \int C_{D,YZ}(x) S(x) |v_z(x)| v_z(x) dx \end{array} \right\} \quad [2.3]$$

where S_x is the frontal projection area of the body in the x -direction, $S(x)$ is the cross-section area of the body at x , and (v_x, v_y, v_z) are respectively the components of the flow velocity at x in the x , y , and z -directions. In the above, $C_{D,x=\pm L/2}$ are the longitudinal viscous drag coefficients of the body at the front ($x=L/2$) and rear ($x=-L/2$) ends, and $C_{D,YZ}(x)$ is the transverse drag coefficient of the body [28]. The distribution of the drag coefficient along the body is modeled based on available experimental data. The detailed description of the modeling is given in section 3.1.

An accurate evaluation of environmental forcing on the body requires solving the complete hydrodynamic problem of wave-body and wave-current interactions. This is

feasible in principle by using numerical methods but is computationally expensive for practical application. Since the length scale of mines is much smaller than that of variable current and typical ocean waves, the excitation force and moment on the body due to current and surface waves can be computed in a straightforward way by neglecting the effect of small body disturbances to the ambient flow.

2.3 Structure of MINE6D

Figure 2.2 summarizes the physics based modeling of MINE6D. The mine characteristic, which includes parameters that describe the body of the mine and the release conditions, are taken as input to the model. First, the body is divided up into small panels. Next the span wise drag coefficient needed in equation 2.3 and the added mass matrix needed in equations 2.1 and 2.2 are generated. The next set of subroutines is repeated for each Monte Carlo Simulation. For a mine entering the water from the air, the impact force and air cavity drag are found. If the mine is deployed in a environment with waves or currents then these forces are calculated. The results from impact, air cavity, and environmental subroutines as well as the drag coefficient and add mass from earlier are used to calculate the hydrodynamic forces for each body panel. The total force is then found on the body and used to evaluate equations 1 and 2. The body's position and orientation are then outputted. If the body has not reached the inputted depth, the time step is advanced and the hydrodynamics are reevaluated based on the previous position. Once the bottom depth is reached the program can repeat the simulation with different randomly chosen release conditions.

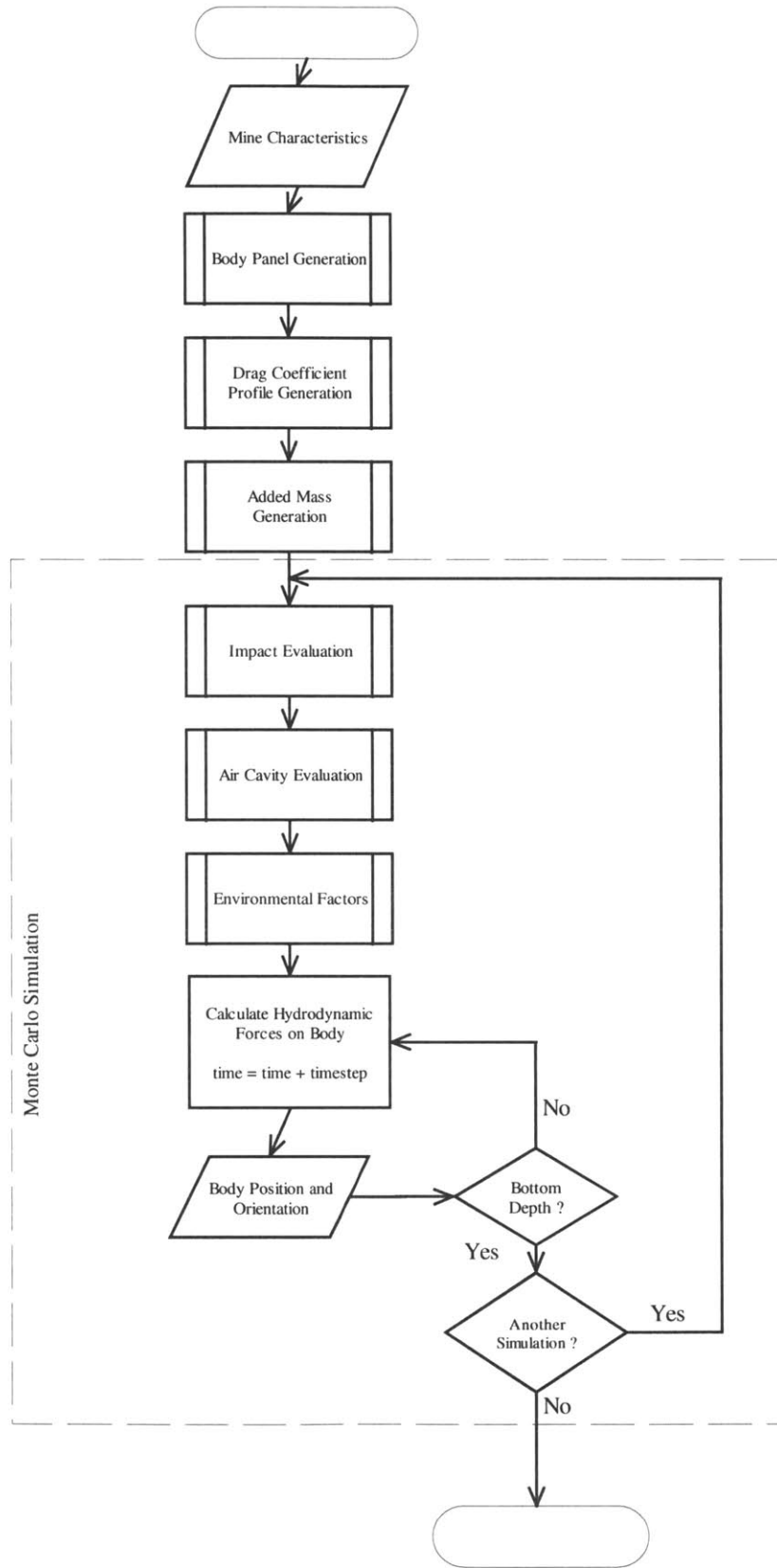


Figure 2.2 MINE6D Flowchart of Physic Modeling

2.4 Predictive Capability of MINE6D

Deterministic MINE6D predictions of mine motions were systematically validated against laboratory experiments conducted at Naval Surface Warfare Center Carderock Division Test Pond in Bethesda, Maryland [21]. For a variety of body (geometry and mass distribution) properties and release conditions, seven distinctive mine motions were identified in these experiments. These motions are categorized as straight, straight-slant, nose-turn, seesaw, tumbling, traveling, and spiral. Figure 2.3 from [21] shows sample trajectories of the mine for see-saw and spiral motions. MINE6D is capable of capturing the essence of each of these characteristic motions. Figure 2.4 shows sample MINE6D predictions of the body trajectories for see-saw and spiral motions. Clearly, the predicted trajectories of the body compare well with the experimental observations. The key characteristics and basic mechanisms of these salient are summarized below.

2.4.1 Straight Motion

Straight motion occurs when the mine maintains a horizontal or vertical orientation throughout the fall. This simple trajectory occurs in calm water when the centers of mass, buoyancy, and added inertia of the body coincide.

2.4.2 Straight-Slant Motion

The straight-slant motion is a pattern for which the body shows a slant movement during a straight fall. The slant movement in the horizontal plane may be caused by ambient flow (such as current) or asymmetric flow separation at the two ends of the mine.

2.4.3 Nose Turn Motion

The nose-turn motion involves the quick change of the orientation of the body. This motion occurs typically when the body drops with an oblique angle or mass center is slightly forward of the buoyancy center. The key mechanism for this motion is associated with the effect of Munk moment and the coupled instability of the sway and yaw motions.

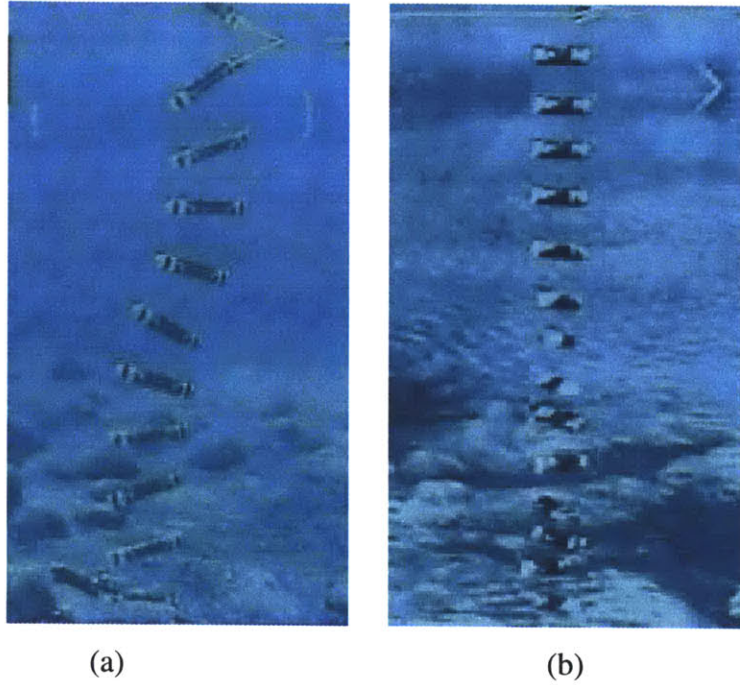


Figure 2.3 Trajectories of the mine observed in tank tests (from Valent et al [21]) for (a) see-saw motion and (b) spiral motion.

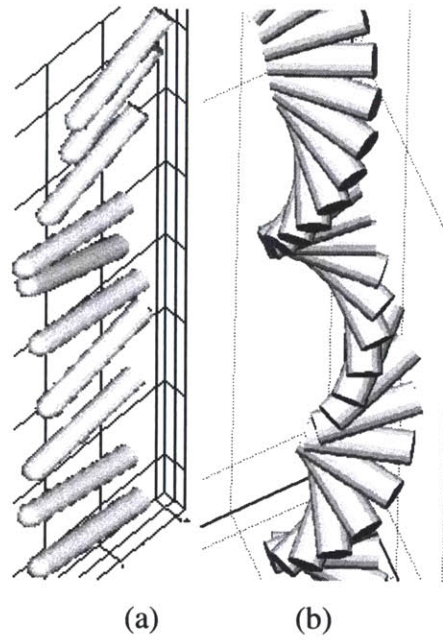


Figure 2.4 Trajectories of the mine predicted by MINE6D for (a) see-saw motion and (b) spiral motion.

2.4.4 See-Saw Motion

When the mass and buoyancy centers are close, pitch oscillation, or “see-saw”, occurs. The mine is seen to pivot around its center. See-saw is the most frequent motion observed in the experiment and direct simulation.

2.4.5 Tumbling Motion

Tumbling motion is seen when the mine flips over itself. For tumbling to occur, the turning inertia after release must exceed the resistance moment due to viscosity and the Munk moment (due to potential flow effect). The mass distribution is an important parameter to triggering the tumbling.

2.4.6 Travel Motion

The travel motion is a stable motion with significant horizontal movement but no significant pitch or yaw rotation. In the experiment, this pattern was observed mostly at oblique drops and the mass centers are somewhat far from the buoyancy center. Under these conditions, the steady oblique angle is sustained to develop the forward horizontal speed.

2.4.7 Spiral

When a cylinder falls through water, a straight or seesaw motion can develop into a spinning motion. This spiral motion is a result from the coupled sway-yaw instability. It may occur when the body experiences sway or yaw disturbance during free fall and/or in the presence of sea-saw oscillation. The characteristics of the spiral motion is similar to those of self-generated spinning, so-called autorotation [10].

2.4.8 Combined

When a cylindrical body drops in a non-uniform flow environment, the body can experience combinations of the previously described motions. The combination and sequence of motion patterns are dependent on a variety of physical factors including the characteristics of flow disturbances, instantaneous motion attitude and velocity, body geometry, and mass distribution. Since the practical flow environment is highly varied and sometimes even chaotic, reliably predicting the details of the combination motion of a mine can be difficult.

Chapter 3

Modeling of Key Dynamic Processes

In addition to accurately predicting the key characteristic features of the mine motion under well-controlled environments, MINE6D can account for the hydrodynamic effects of complex physical processes involved in the drop motion of mines in realistic environments using physics-based modeling. The relevant dynamic processes include three-dimensional flow separation and vortex shedding, water impact and air entrainment, and interactions of the mine with current and surface waves. The modeling of each of these processes in MINE6D is described below.

3.1 Computation of Viscous Drag on a Slender Cylindrical Mine

3.1.1 Finite length cylinders in normal flow

Extensive literature exists on the viscous flow around two-dimensional circular cylinders because of its application to pipelines, mooring lines, risers, and oil drilling platforms in offshore engineering. For cylindrical mines, the aspect ratio (i.e. ratio of the cylinder length to the cylinder diameter) is typically less than 15. The vortices shed around the ends of the body significantly influence the wake behind the other parts of the body [11, 23] making the flow inherently three-dimensional. The overall effect is that the drag on a three-dimensional cylinder is smaller than that given by the strip theory based on the two-dimensional result [15, 16, 19, 23]. Such a three-dimensional effect increases as the aspect ratio of the body decreases to a value of 6. For aspect ratios smaller than 6, no further reduction in drag exists [23]. Another consequence of three-dimensional flow is that the drag coefficient is non-uniform along the body. Depending on the geometry of the ends, the drag coefficient near the ends may be larger or smaller than that in the middle portion of the body [19, 23]. Specifically, if the body has blunt ends, strong vortex shedding occurs at the ends. The drag coefficient near the ends is larger than that

in the midsection of the body [7, 23]. If the body has smooth ends that lead to weaker vortex shedding, the drag coefficient near the ends is smaller than that in the midsection of the body [2]. For a cylindrical mine experiencing near-normal incoming flow, the drag coefficient is symmetric about the mid section. Based on the experimental results of Zdravkovich et al. [23] and Hayashi et al. [7,8], this symmetric profile for the drag coefficient is given by

$$C_{D,NZ}(x) = \begin{cases} C_D & \text{if } \bar{\eta} > 2/\pi \text{ and} \\ & |x| \leq \frac{x_0}{2} \\ C_D + C_D \left(1 - \cos \left\{ \frac{\pi}{2(L-x_0)} (2|x|-x_0) \right\} \right) & \text{if } \bar{\eta} > 2/\pi \text{ and} \\ & |x| > \frac{x_0}{2} \\ \frac{\pi}{2} \bar{\eta} C_D + \frac{\pi}{2} \bar{\eta} C_D \left(1 - \cos \left(\frac{\pi}{L} x \right) \right) & \text{if } \bar{\eta} \leq 2/\pi \end{cases} \quad [3.1]$$

where $x_0 = \{L(\bar{\eta} - 2/\pi)/(1 - 2/\pi)\}$, C_D is the in-flow drag coefficient of the two-dimensional cross-section, and $\bar{\eta}$ is the ratio of the three dimensional drag coefficient to the two dimensional drag coefficient. Here $\bar{\eta}$ is a function of the aspect ratio of the body and its value can be obtained based on the data of U.S. Air Force [2].

Note that the profile of the drag coefficient given in equation 3.1 corresponds to the case in which the drag coefficient has a higher value near the ends than it does in the middle section of the body. A localized higher drag coefficient at the cylinder ends is consistent with the results of Luo[11], Zdravkovich et al. [23] and Hayashi et al. [7,8] for finite length cylinders tested without endplates. When endplates are used in an experimental setup, it reduces the flow around the ends and results in a profile where the localized coefficient is lower at the ends [8], creating a convex curve instead of the concave curve described by equation 3.1.

3.1.2 Finite length cylinder in oblique flow

For a cylinder that is orientated at an angle to a uniform flow (or yawed), it is common practice to simply separate the normal and tangential velocity components, based on the

Independence Principle [30]. Though applying the Independence Principle has been shown applicable for two-dimensional cylinders orientated up to 60 degrees from a uniform flow [8], this quasi- two dimensionality does not hold near the ends for a finite length cylinder. When a cylinder is orientated at an angle to the incoming flow, the drag coefficient profile becomes asymmetric. Hayashi et al. [7] has shown this by a series of experiments for a finite circular cylinder with the yaw angles varying between 0 and 30 degrees. When a yaw angle is introduced on a finite length cylinder, the drag coefficient profile takes a large value near the end orientated into the flow, a constant midsection value, and a small value near the end that is pointed away from the flow. The length of the constant midsection drag coefficient value is dependant on the aspect ratio. As the yaw angle is increased, the drag profile remains similar but with a larger maximum drag coefficient and a greater mid-body value. Based on the experimental measurements of Hayashi et al. [7, 8], the drag coefficient profile is approximated by a polynomial representation:

$$C_{D,YZ} = C_D \bar{\eta} L(N + 1) \left(\frac{L}{2} - x^{\frac{N}{L(N+1)}} \right) + C_{D0} \quad [3.2]$$

where N is the order of the polynomial and C_{D0} is the minimum drag coefficient. In practice, the values of N and C_{D0} need to be determined by calibration against experiments or benchmark results. In the results of Hayashi et al. [7, 8] C_{D0} , varied between -0.5 and 0.5 depending on the yaw angle. For simulations presented in this thesis, C_{D0} is assumed to be zero.

The span wise drag coefficients described by equations 3.1 and 3.2 are shown in figure 3.1. The cosine curve is a typical representation of equation 3.1. The linear and cubic curves correspond to equation 3.2 being evaluated with $N = 1$ and $N = 3$ respectively with C_{D0} assumed to be zero. The model can also create a 2-D drag coefficient as described by the uniform curve. Figure 3.1 shows how each profile varies along the length of the cylinder. The uniform and cosine curves are symmetric about the midpoint, while the polynomials are asymmetric.

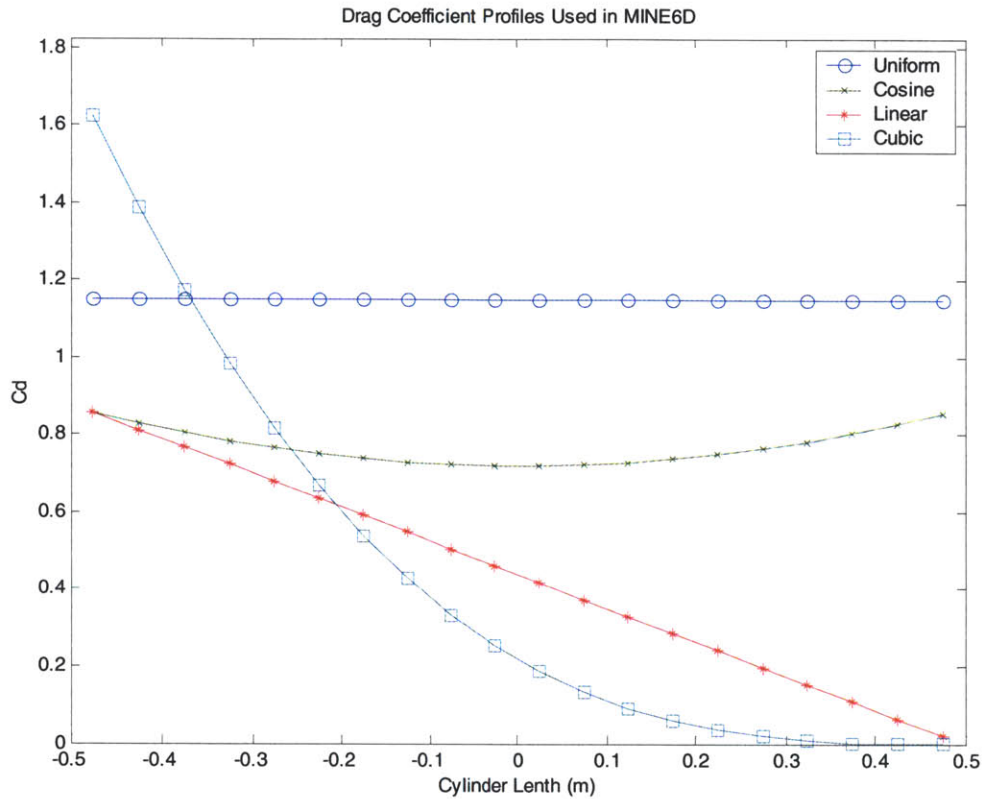


Figure 3.1: Span wise drag coefficient profiles used in MINE6D as given by equations 3.1 and 3.2. The profile used can be user specified.

3.1.3 Sensitivity of mine motions to drag modeling

MINE6D simulations can evaluate the effectiveness of drag modeling. As an example, consider the case of a mine released at an initial oblique angle of 30° with a negative downward velocity of 1 m/s. This mine has a nose, an aspect ratio of 4.5, a specific weight of 1.5, and a center of mass higher than the center of buoyancy. The complete physical parameters of this mine can be found in appendix B, test 18. To show the sensitivity of mine motion to drag modeling, two different drag treatments are analyzed: one assumes a uniform distribution of two-dimensional drag coefficient along the length of the body; and the other uses equation 3.2 with $N=3$ and $C_{D0} = 0$. Figure 3.2 shows the MINE6D predictions of the trajectory and orientation of the mine during its drop in the water. For the case of uniform drag coefficient, the mine exhibits a see-saw motion pattern and converges to a steady horizontal orientation as it reaches its terminal velocity.

For the case of asymmetric distribution of drag coefficient, the mine retains a travel motion pattern with a significantly large pitch angle. Figure 3.3 shows the variation of the velocity of the mine as it drops. The use of asymmetric drag coefficient distribution leads to a larger terminal velocity than that with the uniform drag distribution. These results indicate that in this situation, the drag modeling has a significant effect on the velocity and motion pattern of the mine. The MINE6D prediction with asymmetric drag distribution compares better to the experimental observation in [1].

However not all mine motions show the same sensitivity to drag treatments. For example, heavy mines dropped at (or near) a horizontal orientation from rest have very similar trajectories despite using two different drag treatments: a uniform drag coefficient profile and a cosine drag coefficient profile from equation 3.1. The mine in figure 3.4 has a blunt end, an aspect ratio of 4.5, a specific weight of 2.2, and has a center of mass the coincidences with the center of buoyancy. The complete physical parameters of this mine can be found in appendix B, test 17. As shown in figure 3.4, the effect of the drag treatment is far less dramatic than in figure 3.2. Both the uniform and cosine drag profiles are symmetric. In this situation, the larger specific gravity of the mine dominates the overall motion. The drag treatment does not affect the motion patterns but does influence the magnitude of the vertical velocity, as shown in figure 3.5. This demonstrates that the three dimensional effects in the cosine profile reduces the overall drag when compared to the uniform drag coefficient which represents a two dimensional model. Thus the mine with the cosine drag coefficient profile moves through the circled region faster than the mine with the uniform profile in figure 3.4.

Another case where a lengthwise drag coefficient would have a lesser impact on the mine motion would be for drops about a vertical orientation. As described in the previous section, the location of the center of mass to the center of buoyancy can dominate changes in trajectory for this situation. The mine in figure 3.6 has a nose, aspect ratio of 4.5, specific weight of 1.8, and has a center of mass that is 20% more forward than the center of buoyancy. The mine is released from 38° with an initial horizontal velocity of 1.0 m/s from the surface. The complete physical parameters of this mine can be found in appendix B, test 5. The two drag treatments that are used are the cosine drag coefficient profile from equation 3.1 and the asymmetric drag coefficient

profile from equation 3.2 with $N = 1$ (linear). As shown in figure 3.6, the trajectories appear very similar. Unlike the horizontal release of a heavy mine, the trajectories in figure 3.4 are completed within the same time period. The circled areas highlight the difference. For the cosine symmetric drag coefficient profile, figure 3.6 b, the mine takes a more horizontal attitude during this portion of the fall. For the linear drag coefficient profile, figure 3.6 a, the mine maintains a pitched orientation during this portion of the fall. This difference however does not cause a significant alteration of the bottom velocity and orientation of the mine as demonstrated by figure 3.7. Here the drag treatment is not dominating the motion or considerably influencing any components of the velocity. The forward location of the center of mass from the center of buoyancy prevents the symmetric drag coefficient profile from restoring the mine to a more horizontal orientation.

Despite that only certain motions are sensitive to drag treatment, the proper drag treatment is still a vital component to accurately predict the mine's decent in the water column. The use of a uniform drag coefficient along the length of the mine would fail to capture many of the motions described earlier. Using a symmetric drag coefficient profile for horizontal releases and the asymmetric profile for yawed releases provides a better representation of the drag on a finite length cylinder. However, more experimental data is needed to examine the drag on finite length cylinders. In particular, studies focusing on the drag coefficient profile over a wide range of yaw angles and the effect of pitch oscillations on the drag coefficient would help advance the current model.

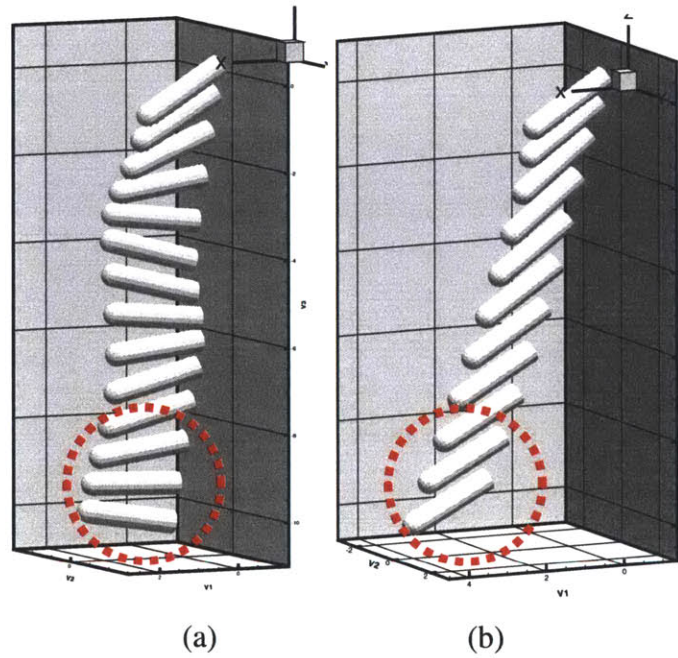


Figure 3.2 Comparison of the effect of drag coefficient treatment on resulting motion. a) A uniform drag coefficient profile is used. b) Cubic drag coefficient profile is used. The cubic drag coefficient has an asymmetric profile that is appropriate for the release angle.

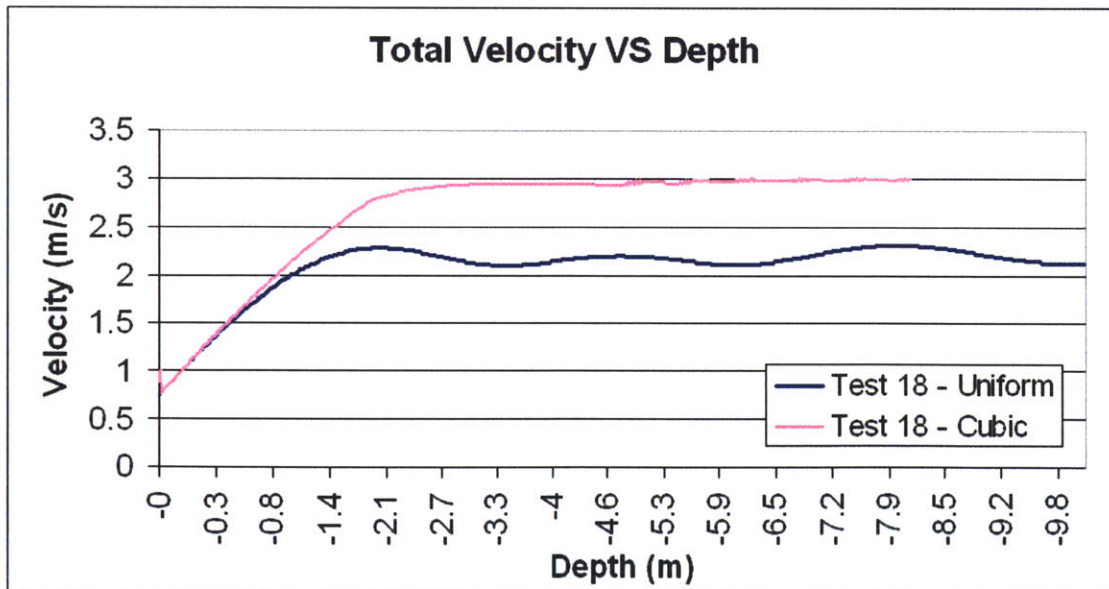


Figure. 3.3 Total Velocity VS Depth for the trajectories shown in figure 3.2

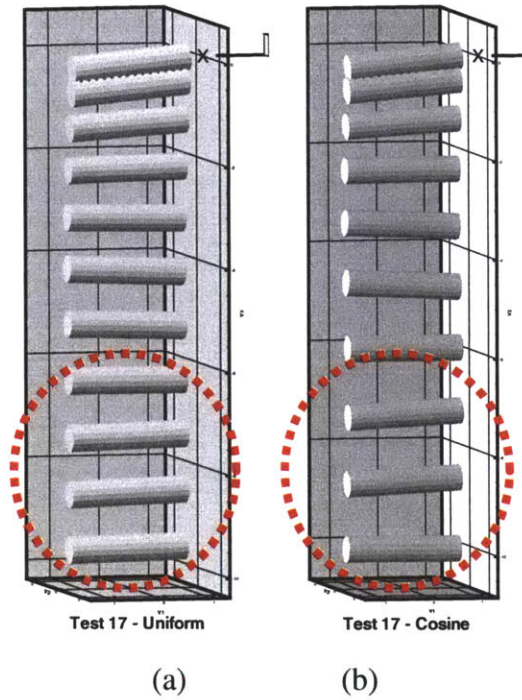


Figure 3.4 Comparison of the effect of drag coefficient treatment on resulting motion.
 a) A uniform drag coefficient profile is used. b) A cosine drag coefficient profile is used. The cosine profile causes the mine to descend more quickly.

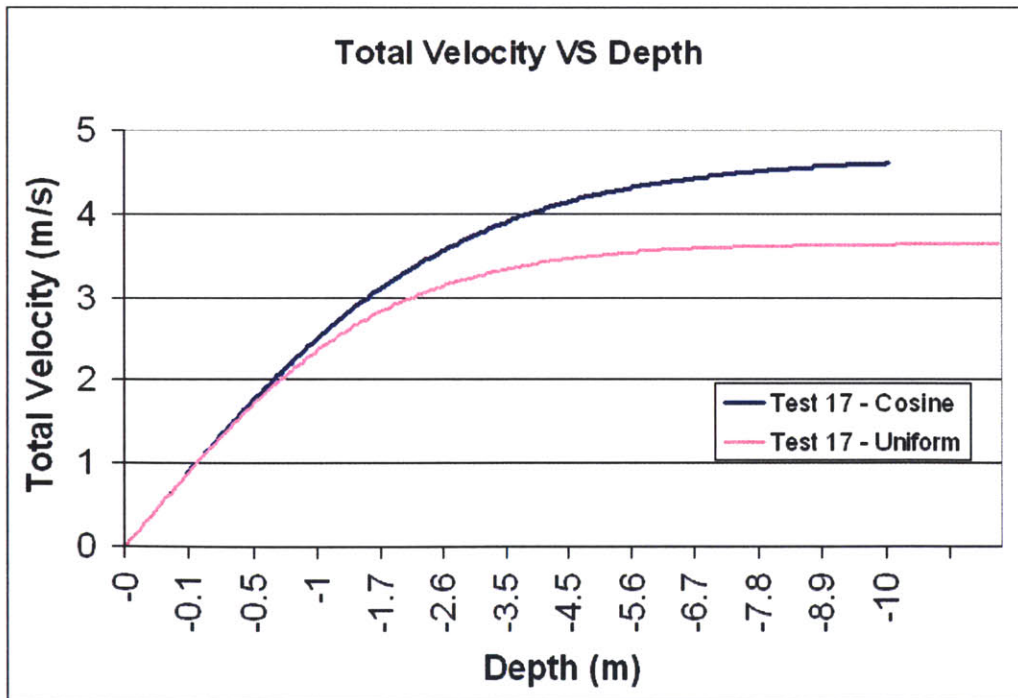


Figure 3.5 Total Velocity VS Depth for the trajectories shown in figure 3.4

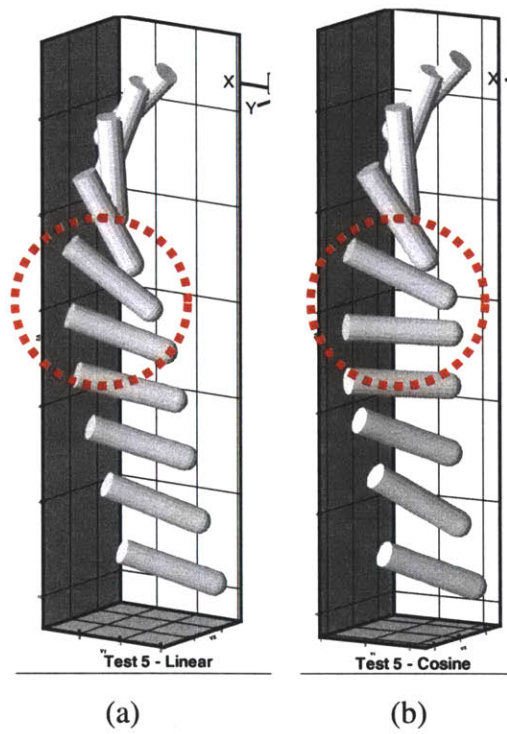


Figure 3.6 Comparison of the effect of drag coefficient treatment on resulting motion. a) A linear drag coefficient profile is used. b) A cosine drag coefficient is used. The different drag treatments do not cause appreciable alterations to the trajectory or velocity.

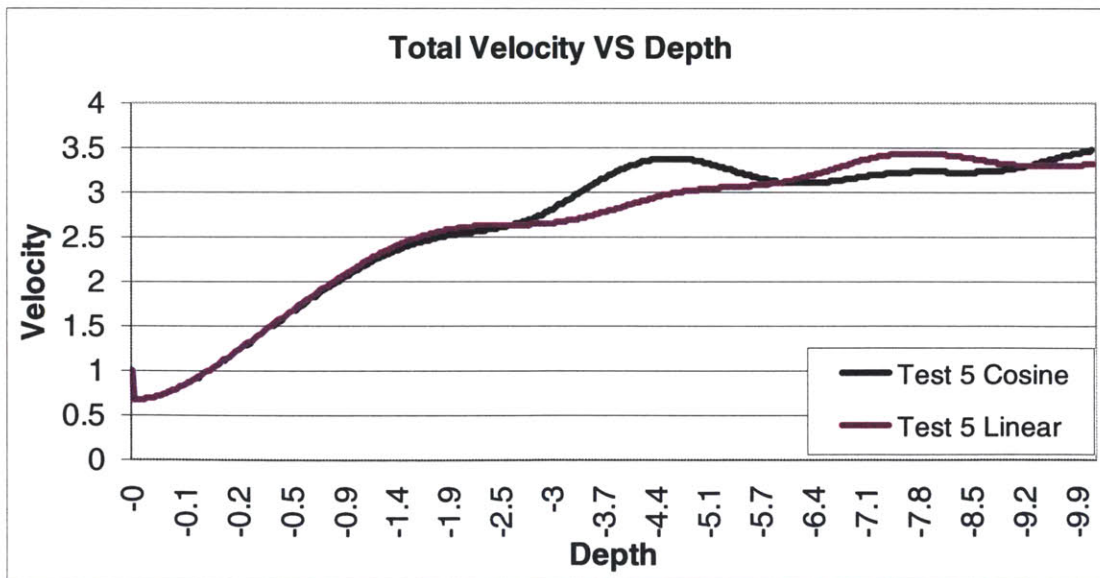


Figure 3.7 Total Velocity VS Depth for the trajectories shown in figure 3.6

3.2 Water Impact of Mines Dropping from the Air

When a mine is released in the air, it experiences a large impact load as it strikes the water surface before it becomes fully submerged and descends toward the sea bottom. During the water impact, the mine loses a significant amount of momentum and its velocity is largely reduced. Accounting for the water impact effect is critical to a reliable prediction of the subsequent mine drop motion in the water.

Various methods from simple asymptotic analysis to complete nonlinear simulations have been developed for the calculation of water impact loads on bodies. Von Karman first developed an asymptotic theory for the flat and near-flat impact problems with the linearized free surface and body boundary conditions. Later, Wagner modified von Karman's solution by accounting for the effect of water splash up on the body during the impact. A generalized Wagner's approach was recently developed by Mei et al [13] based on the extension of the Wagner's asymptotic theory to arbitrary body geometry and entry angle. This approach has been shown to be quite effective for two-dimensional bodies. In addition, nonlinear numerical simulations based on the boundary integral equation have been developed to study the water impact problem including fully nonlinear free surface and body boundary effects [24].

With nonlinear numerical simulations, in principle, the water impact problem can be resolved. However, robust and computationally efficient tools for general three-dimensional bodies are still lacking. Though the similar effectiveness of the generalized Wagner's approach for three-dimensional bodies is expected, the extension to the general three-dimensional impact problem has not yet been developed. At present, MINE6D employs von Karman's analytic model to account for water impact effects.

In von Karman's theory, the hydrodynamic effect of water impact is easily taken into account by properly evaluating the added inertial matrix in the equations of motion of the body, equations 2.1 and 2.2. Specifically, at any instant of impact, the body is approximated by a thin plate whose area is given by the projection of the submerged portion of the body on the mean free surface. The changes in the submerged portion of the body through impact are highlighted in figure 3.8. The added inertial of the body is

then given by that of the plate on the free surface, (which is equal to a half of the added inertial of the same plate in the infinite fluid).

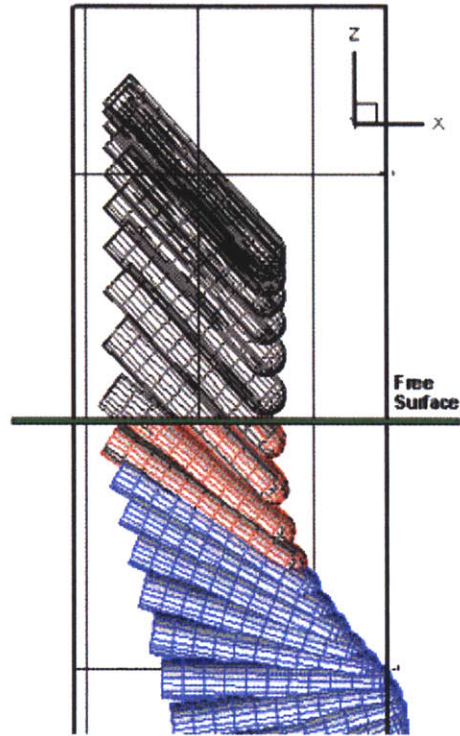


Figure 3.8: Impact of mine with the free surface. The highlighted section in red shows the change in the submerged portion of the body through impact.

3.3 Air Entrainment Cavity Model

3.3.1 Types of Air Entrainment Cavities

After water impact, the mine continues to submerge and move down the water column. Depending on the initial velocity at impact, an air filled cavity may form behind the mine. As body continues down, this cavity pinches off from the surface creating a bubble behind the mine. Prior to pinch off, the air entrainment cavity is open to the atmosphere and subsequently exerts a large force on the mine that retards its motion. This force results from integrating around the surface of the body the differential pressure from bottom half of the mine being surrounded by water and the upper half of the mine being exposed to atmospheric pressure. Therefore, determining the depth at which the cavity

will close from the free surface is important in order to account for the duration of this force. The location of this pinch off is strongly dependent on the (dimensionless) speed at which the body enters the water [3]. Birkhoff and Zarantonello [3] used four different regimes to classify cavity behavior based on entry speed: very low speed, low speed, transient, and high speed. In the very low speed regime ($4.5 < Fr < 8.5$) closure occurs relatively far below the water surface in a deep seal [3]. For low speed entries ($Fr > 12.25$), two distinct pinch offs are observed. The first closure occurs near the surface and then at a later time deep seal is formed [5]. In the high-speed regime, the cavity has a deep seal formation similar to the very low speed is seen. However, this deep seal is a result of airflow into the cavity that delays the pinch off. The airflow into the cavity occurs because the pressure is greatly reduced behind the projectile at these high speeds [9]. For the transient regime there are no available studies that provide a qualitative description of the cavity behavior.

Regime	$Fr = V_i/\sqrt{gD}$	Cavity Behavior
Very Low Speed	$4.5 < Fr < 8.5$	<i>Deep Seal</i> For $Fr \leq 4.5$ cavity may not form
Low Speed	$Fr > 12.25$ No upper limit proposed	<i>Surface Seal Followed By Deep Seal</i> Shown relationship between time for surface seal and time for deep seal
Transient	$Fr > 100$	Not in Literature
High Speed	No lower limit proposed	<i>Deep Seal</i> Due airflow into cavity Large velocity decay may be seen

Table 3.1 Regimes of Cavity Formation Based on the Froude Number

3.3.2 Air Cavity Formation and Model

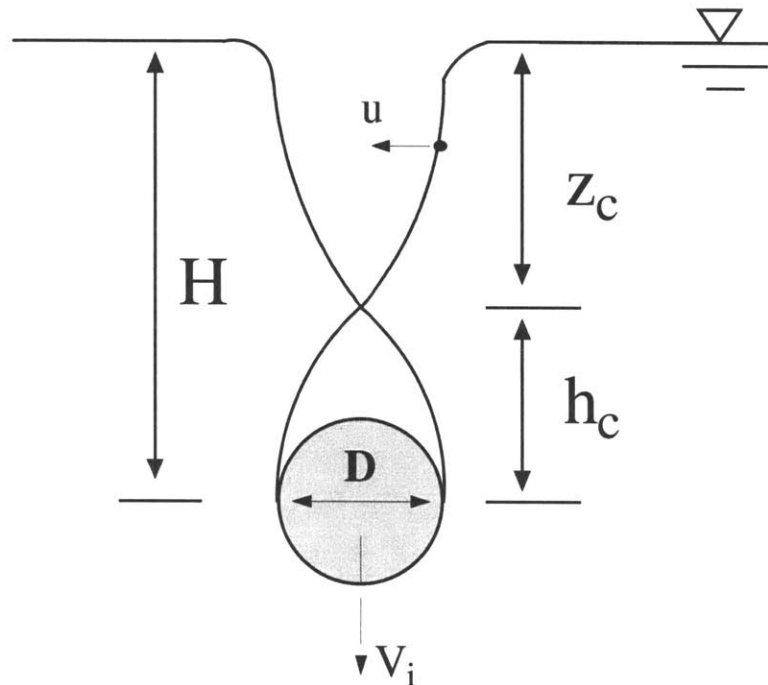


Figure 3.9 The parameters used to describe the cavity formation and pinch off. D is the cylinder diameter. H is the total depth of the cavity to $\frac{1}{2}$ of the top of the cylinder. z_c is depth from the surface where the cavity pinches off. h_c is the height from the pinch off of the cavity to the $\frac{1}{2}$ top of the cylinder. V_i is the velocity of the cylinder downwards. u is the velocity of the cavity wall inward to the middle.

The formation and effects of air entrainment cavities was of particular interest post WW II [5, 12]. For the majority of mine deployments, the impact velocity would be contained within the very low speed regime. Recently, progress has been made in examining cavity behavior for very low speeds [4,6] and high speeds [9,18]. Glasheen and McMahon [6] suggested that the large drag force due to the presence of a cavity could be represented by modifying the drag coefficient. Neglecting surface tension, the drag and modified drag coefficient are expressed as

$$Drag = C_{Dcav} (\frac{1}{2} \rho v(t)^2 S + \rho g H(t) S) \quad [3.3]$$

$$C_{Dcav} = C_D \cdot (1 + \sigma_{we}) \quad [3.4]$$

$$\sigma_{we} = \frac{gH(t)}{\frac{1}{2} v(t)^2} \quad [3.5]$$

where C_D is drag coefficient when cavity is not present, σ_{we} is the water entry cavitation number, H is the length of the cavity, and v is the body velocity.

Including the effect of the cavity within the drag term is attractive because it does not require that boundary value problem be continuously solved for each time step and does not alter the added mass calculations. Applying this modified drag coefficient during cavity formation allows for the cavity model to easily be integrated into the hydrodynamics subroutine of MINE6D. Since this modified drag coefficient however is only appropriate when the cavity is connected to the surface (i.e. before pinch off), the depth at which pinch off occurs must be predicted.

As depicted in figure 3.9, let T be the time from water entry until cavity closure, t_0 be the time from water entry until projectile passes point where cavity will close (z_c), and τ be the time from which the body passes z_c until closure. Then time from water entry of the projectile until cavity closure is given by $T = t_0 + \tau$. From the Bernoulli equation for a point on the cavity wall (while the cavity still open to surface) some distance z below the free surface and a point far away from the cavity on the free surface, the horizontal velocity (u) at which the cavity wall is moving back towards the center of the opening is derived

$$u = \sqrt{2gz} \quad [3.6]$$

The time that it takes the cavity wall to close, τ is then

$$\tau = \delta \frac{D/2}{u} \quad [3.7]$$

where δ is constant based on the projectile shape. T then becomes

$$T = t_0(z) + \delta \frac{D/2}{u} \quad [3.8]$$

The cavity will close when $T(z)$ is minimized. By setting $dT/dz = 0$ and solving for z , an expression for z_c , the depth of cavity closure, can be found. If V_i is assumed constant over the cavity formation then $T = \frac{H}{V_i}$ and $t_0(z) = \frac{z_c}{V_i}$. Plugging in expressions for z_c , T and t_0 gives the following expression for the height of the cavity.

$$H = \left(\delta \frac{DV_i}{4\sqrt{2g}} \right)^{2/3} + \left(\frac{1}{2} \right)^{1/3} \left(\delta \frac{DV_i}{\sqrt{2g}} \right)^{2/3} \quad [3.9]$$

In terms of the Froude Number, $Fr = \frac{V_i}{\sqrt{gD}}$ and a factor, α , that absorbs the remaining

constants the ratio of the height of the cavity to the diameter of the cylinder takes the form

$$\frac{H}{D} = \alpha \cdot (Fr)^{2/3} \quad [3.10]$$

The above analysis assumes that surface tension is negligible; the velocity on the cavity wall is due to only the hydrostatic pressure component; the pressure inside the cavity is atmospheric and that velocity of the projectile is constant through the cavity formation. This estimate of the height of the cavity provided a prediction to within 15 %

for low speed experiments on spheres conducted at the MIT Impact Lab [25] and shown reasonable agreement with the low speed disk experiments of Glasheen and McMahon [6].

At the MIT Impact Lab, billiard balls were dropped into a deep tank with four different initial velocities. A high-speed camera captured the entry of the balls and resulting cavities. The cavity height was then measured from the pixels in the digital photograph. Table 3.2 below summarizes the measured cavity heights and shows the prediction from the model.

Diameter (m)	V_i (m/s)	Fr	H/D	$\frac{H}{D} = 2 \cdot (Fr)^{2/3}$
0.05715	3.00	4.00	5.34	5.05
0.05715	3.39	4.52	5.82	5.47
0.05715	4.06	5.43	5.97	6.18
0.05715	6.77	9.05	7.44	8.68

Table 3.2 Comparison of experimental results with the prediction used in equation 3.10 for a given initial velocity

The drops with initial velocities of 3.00, 3.39, and 4.06 in table 3.2 fall within very low speed classification from Birkhoff and Zarantonello. The last drop however is outside this range. The drops within the very low speed range were the closest to the predicated values. This leads to an important limitation on the proposed theory. It is assumed that the pressure on the cavity wall is atmospheric. This would only be true for object speeds that do not cause a pressure drop in the surrounding air. This is not the case for very high-speed water entries and thus the model is limited to the very low speed regime.

Since no controlled experiments for cylindrical shapes at low Froude numbers was available, the model was compared to the low speed entry disk experiments conducted by

Glasheen and McMahon [6]. Figure 3.10 shows a plot of their experimental data for the relative air cavity closure height (cavity closure height / radius of the disk) versus the Froude number and the predicted values of the air cavity model based on the $Fr^{2/3}$. The coefficient, α was adjusted from 2 to 1.45 to reflect the difference in body shape. Again, the lower the Froude number, the better the model compares with experiments.

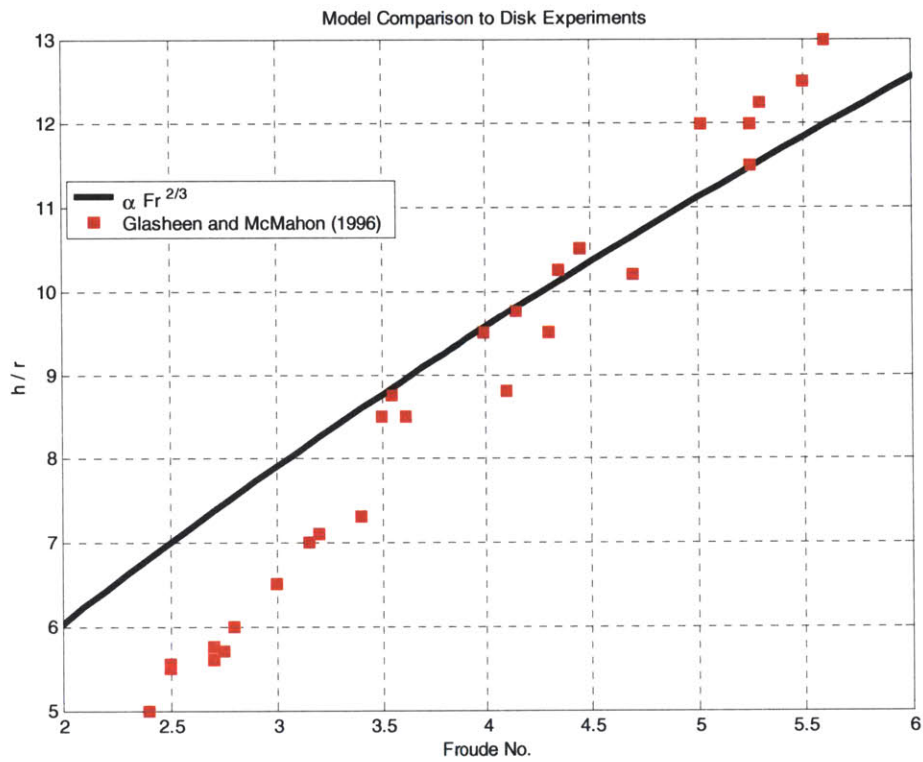


Figure 3.10: Comparison of air cavity model to disk experiments conducted by Glasheen and McMahon [6] for low Froude numbers. $\alpha = 1.45$

3.3.3 Bubble After Cavity Closure

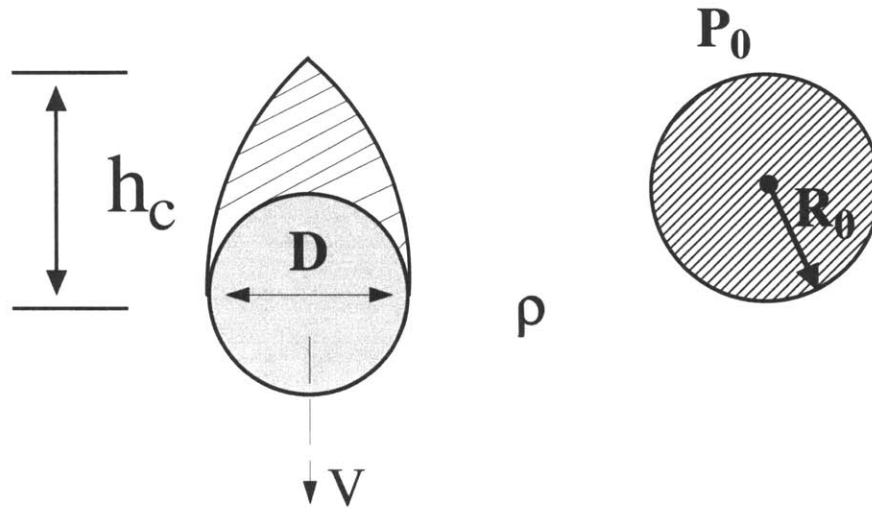


Figure 3.11 On the left is the bubble after pinch off. On the right is the equivalent volume spherical volume.

After cavity closure occurs, the cavity volume below the pinch off is attached and moving with mine. A portion of the cavity is now a bubble and is not open to the atmosphere. Though closed from the free surface, the bubble still exerts a significant force on the body. As shown in the experimental data in figure 3.14, after the cavity pinches off the bubble collapses and expands, causing an oscillation in the body's acceleration. This rate of collapse and expansion is determined by the natural frequency of the bubble. To model the bubble, the equivalent spherical volume is calculated from the total cavity height, the relative pinch off location and the mine's dimensions. The mine's dimensions are given as input and the cavity height is found from equation 3.10. The relative pinch off location is given as $2/3$ of the total cavity height below the free surface. This empirical value of $2/3$ was determined from drops completed at the MIT Impact Lab [25]. Like the data presented in table 3.2, the heights were measured from pixel distances from digital photographs taken with a high-speed camera. It should be noted that the $2/3$ value is a result obtained from experiments on spheres. The natural frequency of a spherical bubble is given by [27]

$$\omega_n = \sqrt{\frac{3P_0\gamma_a}{\rho R_0^2}} \quad [3.11]$$

Where R_0 is the radius of the equivalent sphere, P_0 is the external pressure at cavity closure, ρ is the density of the surrounding fluid, and γ_a is ratio of the specific heats for the gas.

This expression from Minnaert [27] assumes small amplitude oscillations of an adiabatic spherical bubble rising in a quiescent fluid. In an actual drop, the bubble behind the mine is not a constant volume and not spherical. As the mine drops, the large bubble collapses and releases smaller bubbles in the wakes. This creates a cloud of bubbles around the mine. However, this expression for the natural frequency of the bubble has reasonable agreement with the experiments conducted at the Model Basin Pond [17] as shown in table 3.3. The time till cavity closure and natural frequency in table 3.3 were measured from the vertical accelerometer measurements taken during field experiments [17]. For the predicted natural frequency, R_0 and P_0 were estimated using the release orientation (vertical or horizontal), the dimensions of the mine and 1/3 of the closure depth (i.e. the remaining third of the total cavity height below the pinch off depth). The depth was assumed based on the time of cavity closure and impact velocity. The impact velocity was calculated from the height of release above the water, usually of a distance of 1 meter. The oscillation of the bubble is significant because it appears in the vertical acceleration of the mine. After the cavity pinches off, the acceleration of the mine decays as an oscillating exponential as can be see in figure 3.14.

Measured Time of Cavity Closure	Measured ω_n (NGLI Site)	Predicted ω_n (eq.)
0.035	0.043	0.046
0.048	0.060	0.053
0.054	0.060	0.052
0.347	0.068	0.072
0.379	0.074	0.072
0.368	0.075	0.072

Table 3.3 Compares measured bubble oscillations from NGLI Site Experiments and the predicted bubble oscillation from equation 3.11. The measured time of the cavity closure was used to determine the radius of the bubble for the predicted value.

3.3.4 Modeling of air entrainment in MINE6D

MINE6D uses equation 3.10 to predict the height of the cavity based on the velocity of the body after water impact. The drag coefficient is evaluated according to equation 3.4 until the mine passes the predicted height. As shown in equation 3.5 the drag coefficient increases as the length of the cavity increases prior to deep closure. The physical parameters of the mine used in the simulations shown figures 3.12 through 3.15 can be found in appendix C under mass-1. A horizontal release orientation is used to match the experimental conditions.

The model of the cavity prior to pinch off is compared to experimental data in the figure 3.12. First, the acceleration decreases by 0.5 g while the cavity is present. In this model, the cavity was predicted to be present for 0.5 second compared to 0.52 second in the experiment. During this period of time, the velocity of the mine decreases significantly. While it confirms that the cavity's presence is significant to the mine motion, it shows the weakness in assuming the velocity is constant through the cavity formation. In figure 3.13, the resulting motion is shown for a drop with an air cavity formation and without an air cavity formation. Compared to the motion without the inclusion of the cavity effect, the mine falls more slowly and the translational motion is more damped.

In figure 3.14, the model of both the cavity and the bubble after closure are compared to a field experiment [17] and to the MINE6D model without the inclusion of the cavity and bubble models. The time until closure, the bubble oscillation, and bubble decay rate of the model show good agreement to the field experiment. After pinch off, the oscillation and decay of the bubble are modeled by the following modification to the cavity number in equation 3.4.

$$\sigma = \sigma_{we f} \cdot e^{\beta(t-T_0)} \cdot \cos \omega_n (t - T_0) \quad [3.12]$$

where σ replaces σ_{we} in equation 3.4, $\sigma_{we f}$ is the value of the cavitation number at cavity closure, β is the decay rate of the bubble, T_0 is the time of cavity closure, ω_n is the natural frequency from equation 3.11, and t is the time.

In general, the decay rate, β needs to be calibrated by experimental results since it may depend on the orientation at impact, the aspect ratio, the roughness of the surface and the impact velocity. The accelerometer measurements from 5 drops (NGLI Site 9 drops 8, 9, 11, 12, and 13) with a horizontal release of the same mine at one meter above the surface all show a similar decay rate [17] of $\beta = 13$. The effect of decay rate on the acceleration is shown in figure 3.15. Three different decays are shown for the same drop: $\beta = 5, 13$ and 25. The larger the β value is, the more quickly the bubble oscillation dies out. Though a β of 13 was determined from experiments for horizontal drops, a different β value may be useful for oblique drops or different shaped mines.

The model's mean acceleration during the bubble oscillation however is under predicted compared to the field experiment. The MINE6D curve without the air cavity model shows how much is missed if the air cavity and bubble oscillation are disregarded. In fact, within the time presented in the figure, the model without the air cavity and travel more than twice as deep than the field experiment or model with the air cavity and remaining bubble.

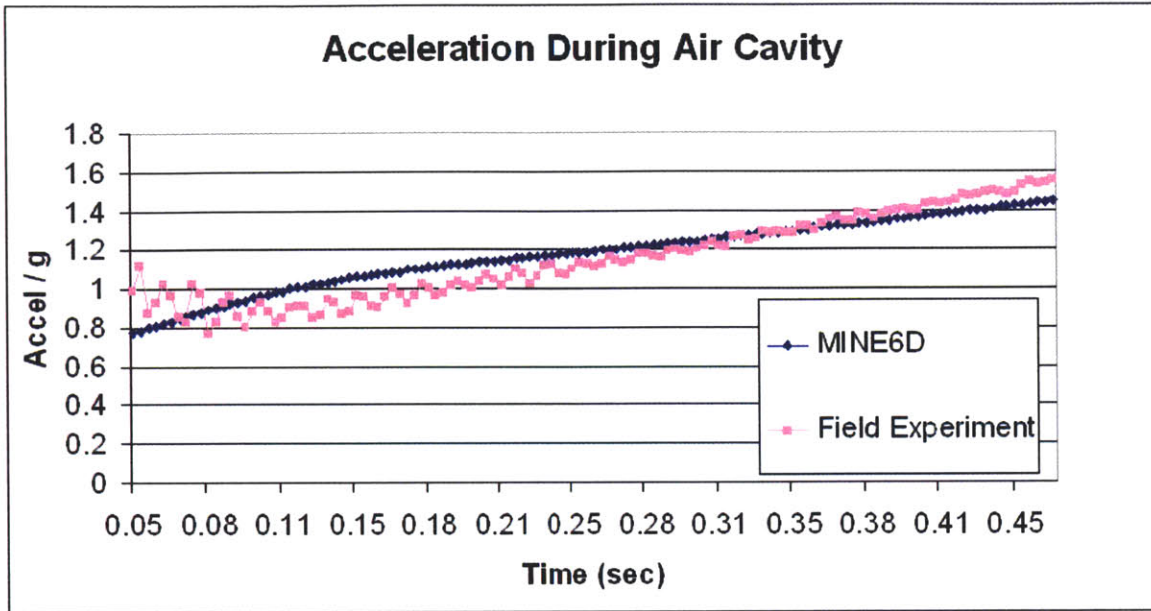


Figure 3.12 Comparison of the acceleration with the cavity and an experiment from NGLI Site 9, Drop 8 [17]. The cavity model shows the dramatic deceleration while the cavity is present.

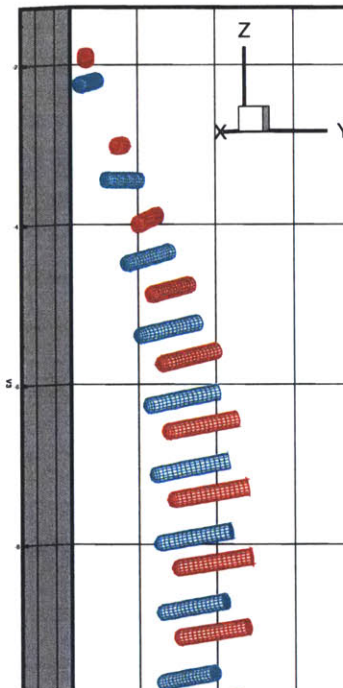


Figure 3.13 Visualization of the comparison of the cavity model (dark red) and non-cavity model (light blue). The cavity model descends more slowly and has less translational motion.

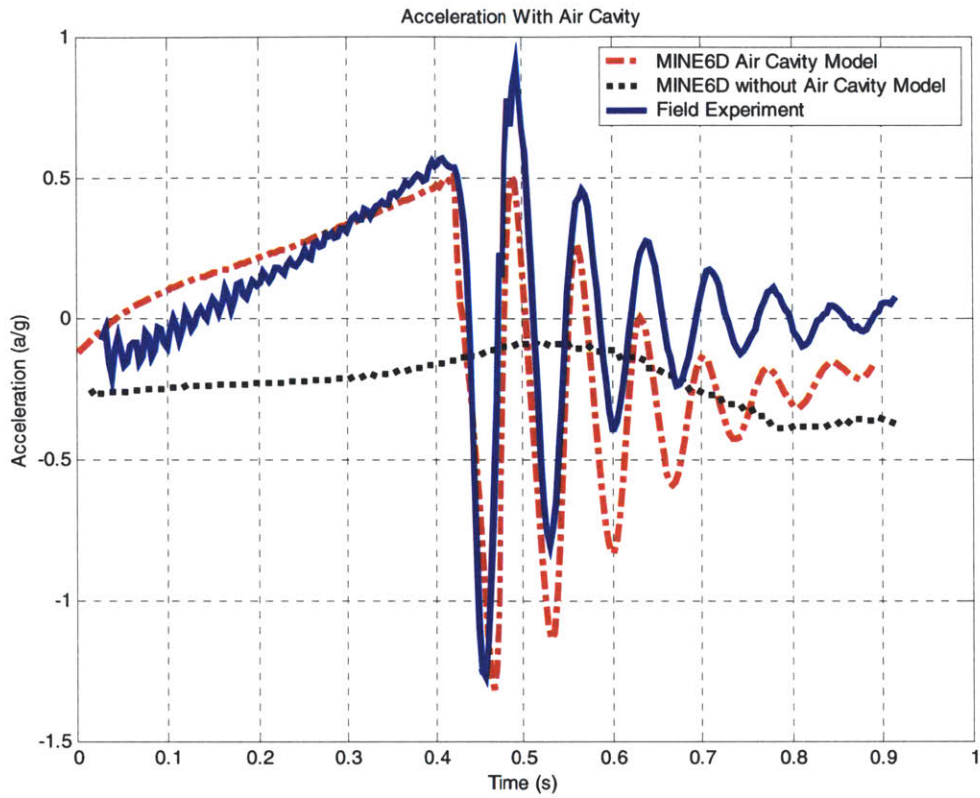


Figure 3.14 Acceleration of mine with air entrainment, comparison of acceleration for a field experiment (NGLI Site 9, Drop 8B) with an air cavity is formed from the drop to MINE6D with the air cavity and bubble model ($\beta = 13$) and to MINE6D without air cavity consideration. The cavity is open to air between 0 and .425 seconds. The cavity closes and a bubble follows the mine from 0.425 seconds and 0.8 seconds.

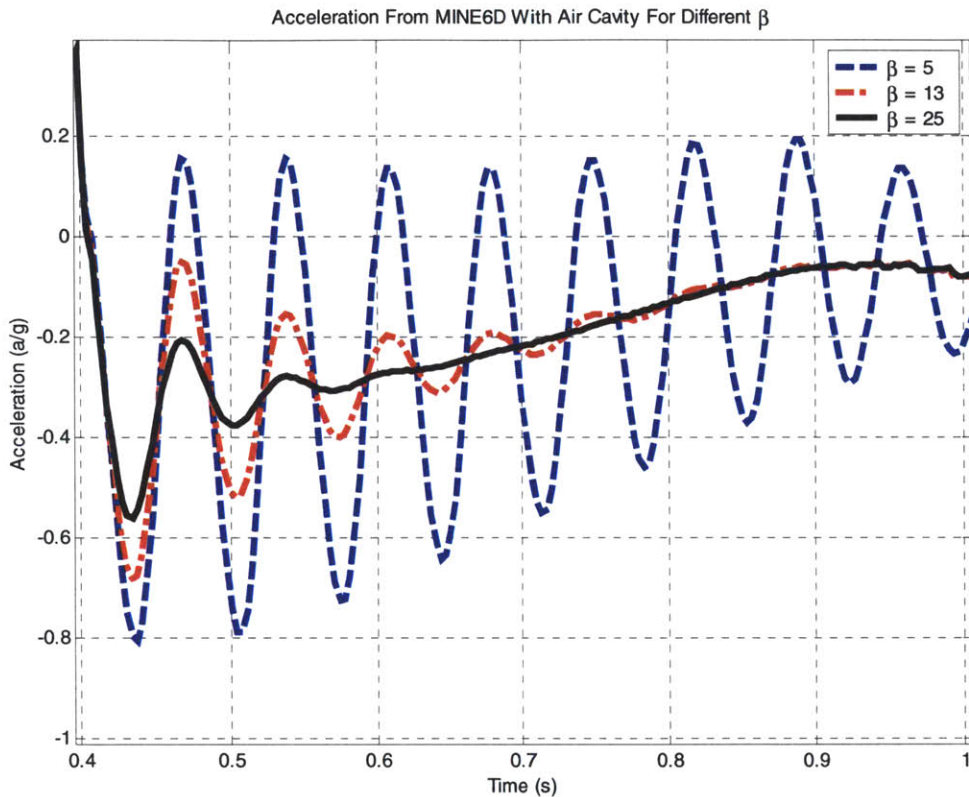


Figure 3.15 Acceleration with MINE6D bubble model for differing decay rates, $\beta = 5, 13,$ and 25 . The time shown is from cavity closure forward. The higher the β value is, the faster the decay of the bubble. β needs to be calibrated against experimental results.

3.4 Environmental Conditions

In the deployment of mines, mild surface waves and variable current may be present in the sea. Since the length scale of mines is much smaller than the characteristic length scale of typical ocean waves and current, the disturbance of the body to ambient flow can be neglected. The hydrodynamic loads on mines as a result of these environmental conditions can be found using the G.I. Taylor long wavelength approximation.

Ambient current can have a dramatic effect on the trajectory of a falling mine. Figure 3.15 shows the comparison of the MINE6D prediction to the field measurement for the trajectory of a mine in the presence of a deep current. As shown in figure 3.15b, the mine

sees a large translational movement due to the effect of a simple current acting along one direction. Currents that have additional velocity components and occur over a wide depth range can induce additional mine motions than would otherwise be seen. Figure 3.15 a shows the visualization from a field test completed at Cocrdrie, LA [1]. The comparison between the MINE6D prediction and the field measurement demonstrates the necessity to include ambient environment effects in practical applications of MINE6D.

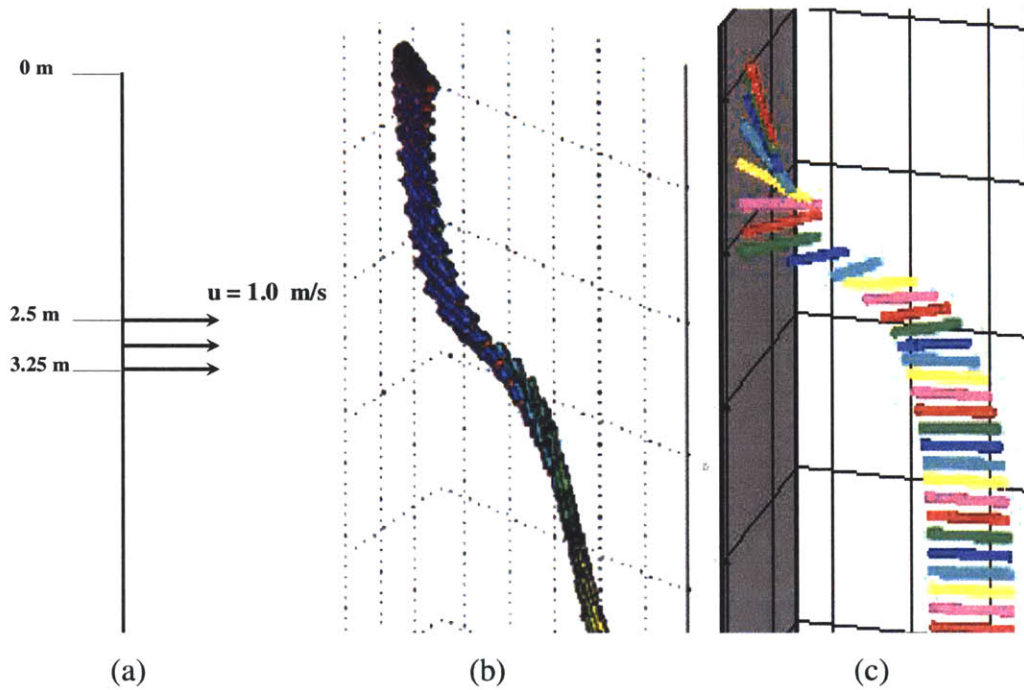


Figure 3.16 Environmental Effects

- a) Current Profile Used in MINE6D
- b) From Abele v[1] Presence of current in field test in LA
- c) Presence of current in MINE6D

Chapter 4

Statistical Descriptions of Mine Motion

The ultimate objective of developing a reliable deterministic model is to provide transfer functions of the velocity and orientation of the mine near the bottom as a necessary input to a stochastic mine burial prediction model. Since the dynamics of mine drop motion in the water is quite sensitive to a large number of physical parameters and the practical environments are highly irregular, it is useful and necessary to employ a stochastic model to establish the characterization of mine motion patterns. A stochastic model also provides a means of representing the uncertainties associated with a real mine deployment. Finally, this model can be extended as a design tool.

4.1 Monte Carlo Simulation

For a linear, time invariant system it is possible to predict the system output in terms of the input and a transfer function [31]. Mine dynamics, however, is neither linear nor time invariant system. Instead of trying to obtain an analytic transfer function for a mine's descent, it is more practical to provide a stochastic transfer function. In the situation of predicting mine burial of enemy mines, the exact values of the mine's physical parameters, the mine's release conditions, the deployment environment will not be known. In this case, it would be useful to express the percent certainty of the system output (bottom velocity and orientation) based on a probable input. Thus, a statistical description of mine motion is more powerful than just the deterministic model. In order to obtain a stochastic transfer function it is necessary to analysis the results of numerous simulations over a wide range of input conditions. To achieve the statistical input and output comparison, MINE6D uses a Monte Carlo Direct Simulation to auto generate numerous runs. The Monte Carlo method uses a sampling of random numbers to generate inputs for a specified number of simulations [26]. Though the methodology

behind the Monte Carlo Simulation method has been known for centuries it has gained recent popularity in many fields due to availability of faster computer processors [14]. The sampling of random numbers is controlled by a probability density function (PDF). MINE6D uses a Gaussian distribution given by

$$f_X(x) = \frac{1}{\sigma_X \sqrt{2\pi}} e^{-\frac{(x-\mu_X)^2}{2\sigma_X^2}} \quad [4.1]$$

$$f_Y(y) = \frac{1}{\sigma_Y \sqrt{2\pi}} e^{-\frac{(y-\mu_Y)^2}{2\sigma_Y^2}} \quad [4.2]$$

where μ_X and μ_Y are the means of the initial horizontal velocity and the initial angle of orientation from the vertical, respectively and σ_X and σ_Y are the standard deviation of the initial horizontal velocity and the initial angle of orientation from the vertical, respectively. The random variables, x and y are determined using the CPU's clock. The time provides a seed which is used to generate the number of standard deviations from the mean to produce x , the initial horizontal velocity and y , the initial angle of orientation.

Figure 4.1 shows the randomly generated initial horizontal velocity when a mean of 0.5 m/s and a standard deviation of 0.25 m/s are specified. Figure 4.2 shows the randomly generated initial angle of orientation from the vertical when a mean of 45 degrees and a standard deviation of 30 degrees are specified. In both figure 4.1 and 4.2 the corresponding Gaussian distribution, as given by equations 4.1 and 4.1, is plotted over the histogram. This demonstrates that the randomly selected values do represent a Gaussian distribution. Though the initial horizontal velocity and initial angle were used in this study, this concept can be easily extended to other physical parameters of the mine's release.

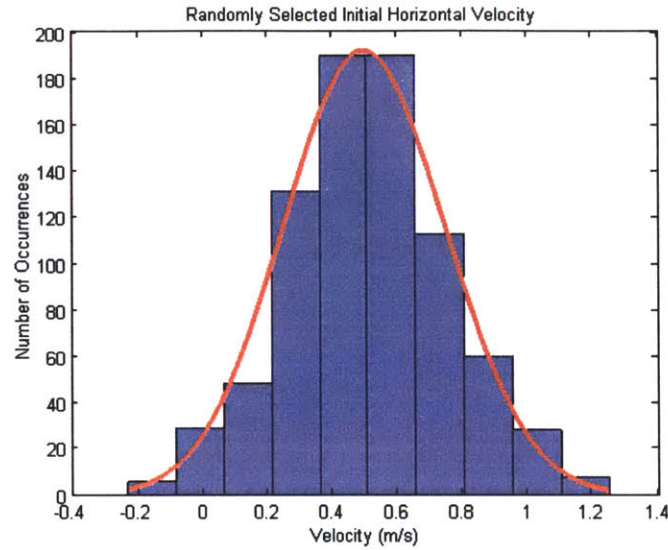


Figure 4.1 Histogram and Gaussian PDF of the initial horizontal velocity. The specified μ_X is 0.5 m/s and σ_X is 0.25. The scaled Gaussian PDF for the specified mean and standard deviation plotted over a histogram of 800 random variables created for the Monte Carlo Simulation.

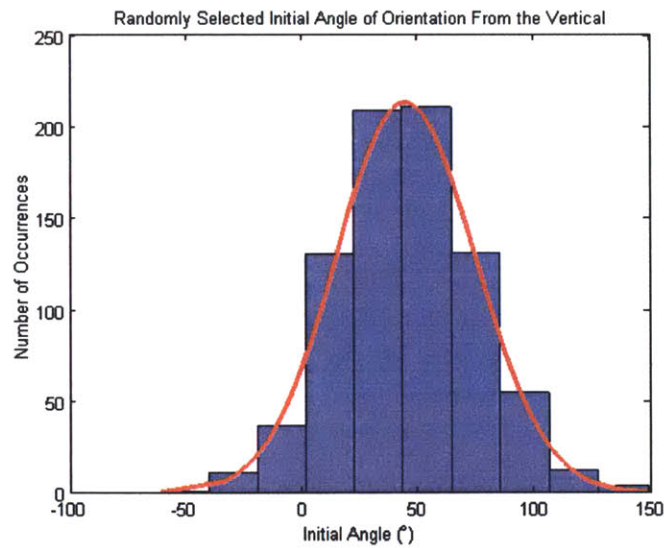


Figure 4.2 Histogram and Gaussian PDF of the initial angle. The specified μ_Y is 45 degrees and σ_Y is 30 degrees. The scaled Gaussian PDF for the specified mean and standard deviation plotted over a histogram of 800 random variables created for the Monte Carlo Simulation.

The randomly chosen horizontal velocity and angle serve as input into the MINE6D deterministic model. For each desired simulation, a new x and y are chosen and the simulation is rerun. Since this input is statistically controlled, it allows for a stochastic transfer function determined by the mean and variance of the input and output. Furthermore, generating numerous simulations provides a measure of sensitivity of the output on a specific input parameter.

4.2 Statistical Characterizations

Basic statistical information and depth-averaged quantities can be obtained from the MINE6D Monte Carlo Simulations. At desired depths, the mean and standard deviation is found over all the simulations for the velocity and rotational components. For example, the user can examine the mean and standard deviation of the pitch velocity near the beginning of the drop, midway through the drop, and at the bottom of the drop.

The statistical information gathered from numerous simulations is useful for assessing trends in the motions. These trends can evaluate the sensitivity of motion patterns to a certain physical property of the mine such as bulk density or location of center of mass [28].

4.2.1 Characterizations of Different Drag Coefficients

In order to further examine the importance of the drag treatment, two hundred simulations were run for four different drag treatments: a uniform drag coefficient, a cosine symmetric drag coefficient profile as given by equation 3.1, a linear drag coefficient profile as given by equation 3.2 with $N = 1$, and a cubic drag coefficient profile as given by equation 3.2 with $N = 3$. The mine in this simulation had a nose, an aspect ratio of 6.4, and a specific weight of 1.9. The detailed physical parameters can be found in appendix C, mass 9. The simulations covered release conditions with relatively large standard deviations. The release angle had a mean of 45° and a standard deviation of 30° as shown in figure 4.2. The horizontal velocity at release had a mean of 0.5 m/s and a standard deviation of .25 m/s has shown in figure 4.1. Instead of looking at each individual trajectory, the histogram, mean and standard deviation of the bottom velocity

and bottom pitch angle are more useful in establishing a trend. In figures 4.3, 4.4, 4.5 and 4.6 a histogram of the bottom velocity is shown for each drag treatment. In figures 4.7, 4.8, 4.9 and 4.10 a histogram of the bottom pitch angle is shown for each drag treatment. Finally, table 4.1 summarizes the mean and standard deviation of the bottom velocity and pitch angle for each drag treatment.

The symmetric cosine drag coefficient profile is an improvement of the 2-D uniform drag coefficient model. Based on the histograms, means and standard deviations, a 2-D uniform drag treatment is unable to predict higher bottom velocities and larger impact angles. The cosine symmetric drag treatment however provided the largest spread in bottom velocities and impact angles. This spread suggests that a variety of motion patterns are encountered over the simulations, confirming that symmetric drag profile is a substantial improvement to a 2-D drag treatment.

The linear drag coefficient profile offers a simple model to account for the experimental asymmetry in drag for yawed cylinders. This linear approximation decreases the deviation of the bottom velocity as compared to the symmetric cosine treatment and dramatically reduces the impact angle of the mine. The cubic drag coefficient profile improves on the linear approximation as is closer to the curves measured by Hayashi et al [7]. The cubic profile has the largest bottom velocity out of all the drag treatments and the smallest deviation. It also provides the largest impact angle as well. The cubic profile achieves higher bottom velocities and impact angles that have been observed in experiments [23]. Overall, the results for each drag treatment reinforce that using a 2-D approximation is inadequate in representing mine motion. Furthermore drag treatment appropriate to the initial release conditions is necessary for reliable prediction since the symmetric and asymmetric profiles together capture the complete range of mine motion.

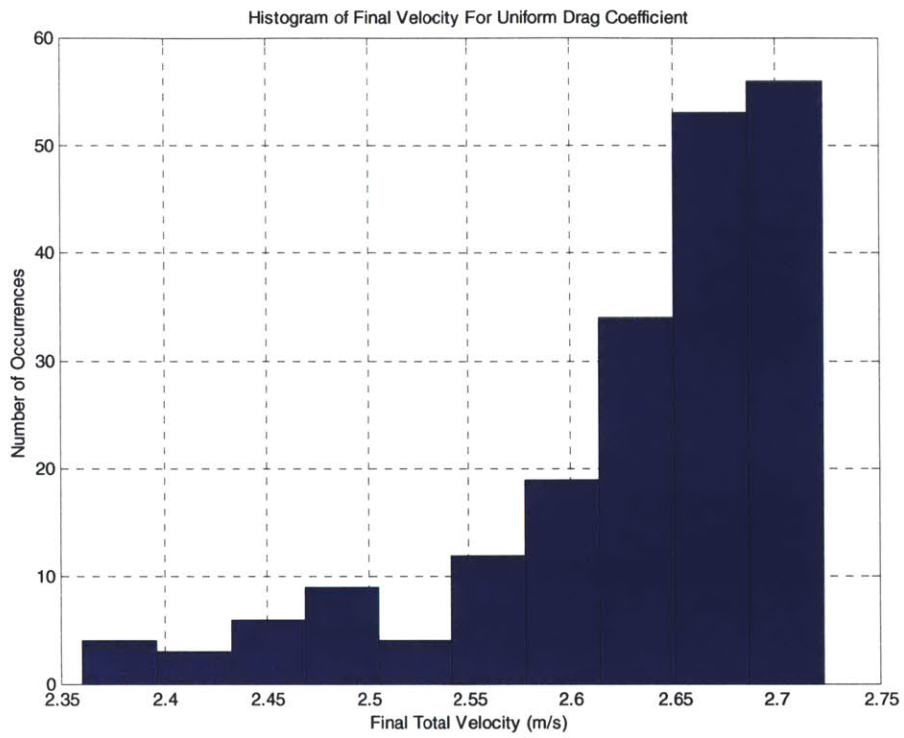


Figure 4.3 Bottom velocity histogram for uniform drag treatment for 200 simulations

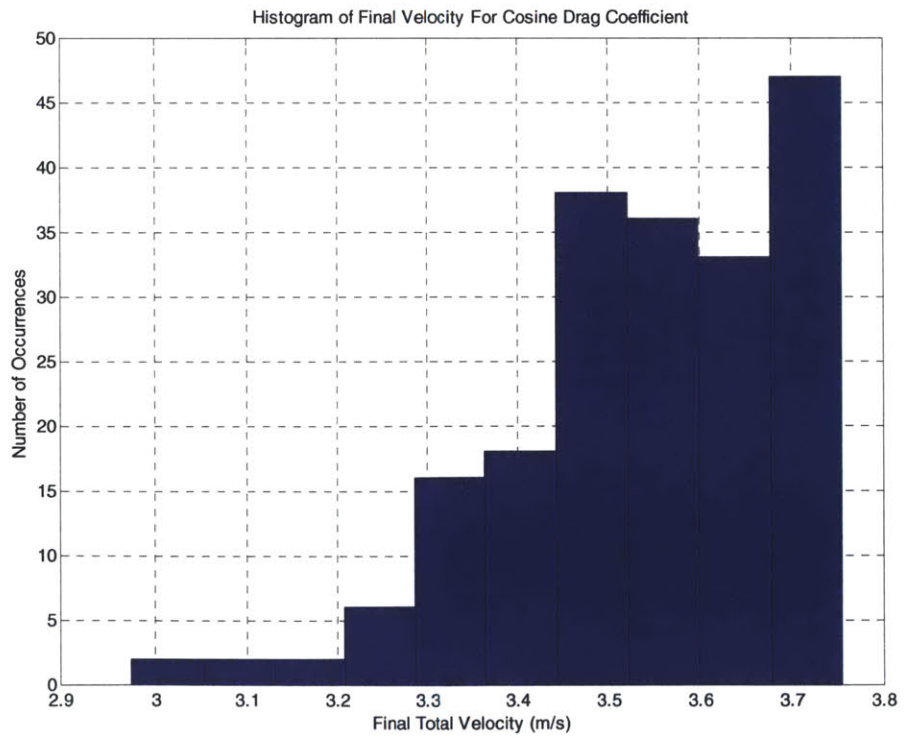


Figure 4.4 Bottom velocity histogram for cosine drag treatment for 200 simulations

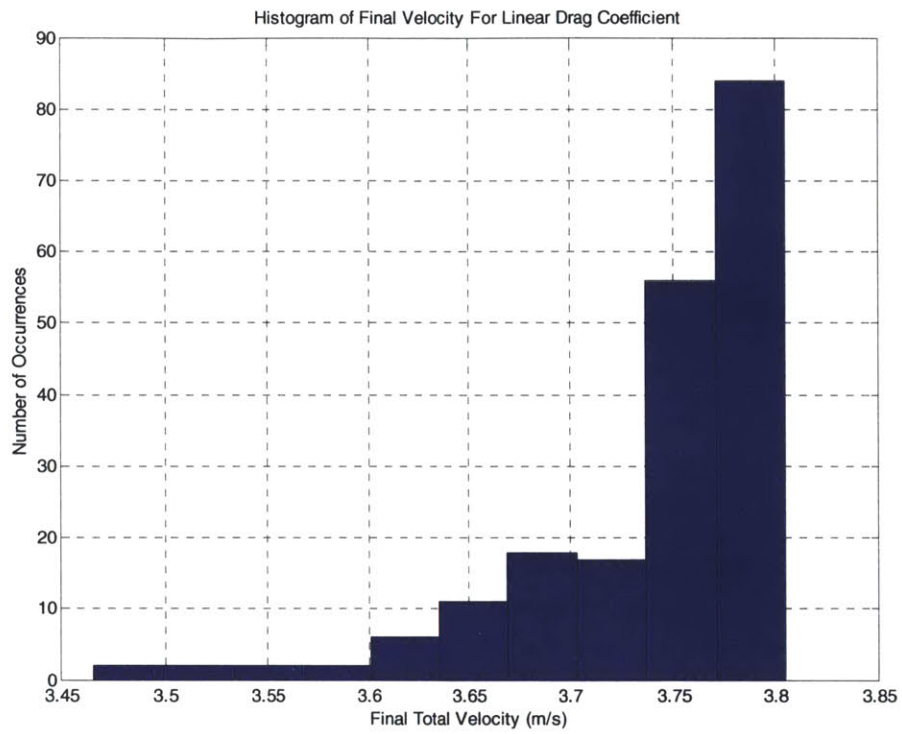


Figure 4.5 Bottom velocity histogram for linear drag treatment for 200 simulations

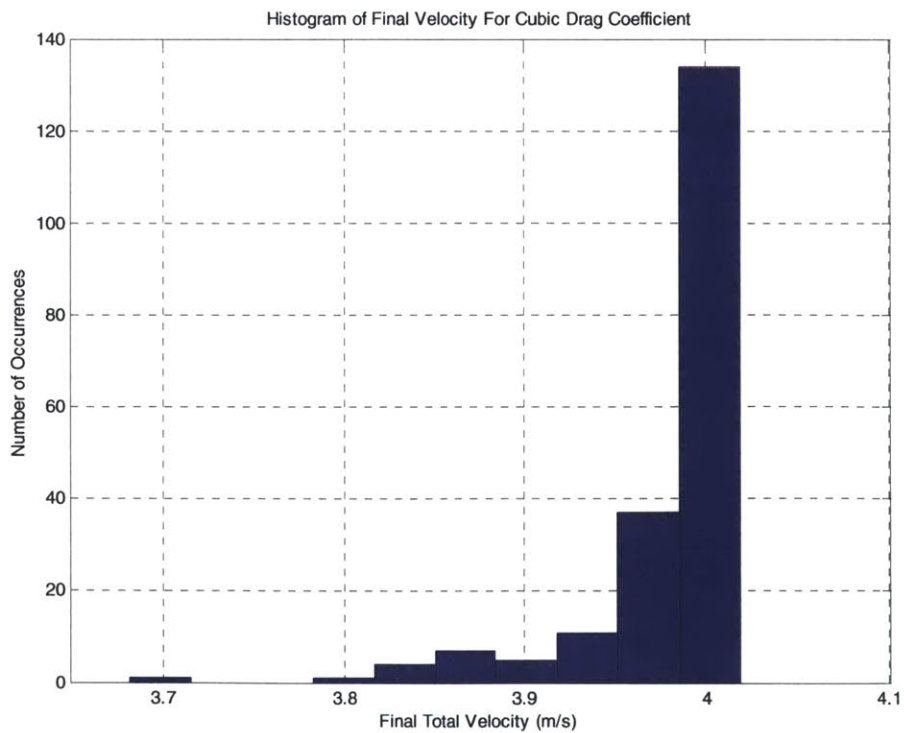


Figure 4.6 Bottom velocity histogram for cubic drag treatment for 200 simulations

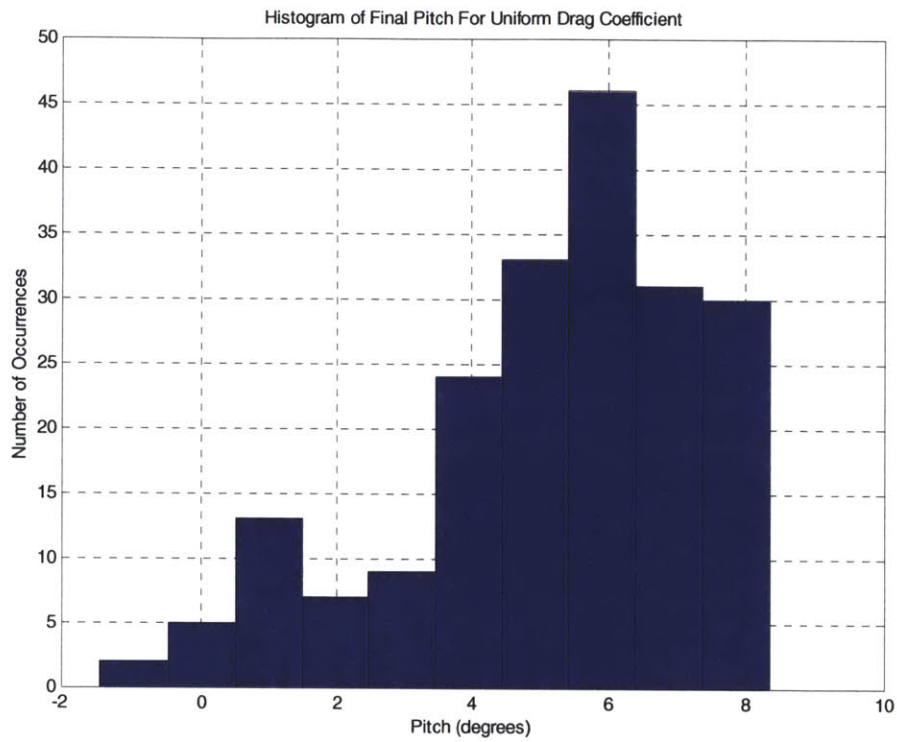


Figure 4.7 Bottom pitch angle histogram for uniform drag treatment for 200 simulations

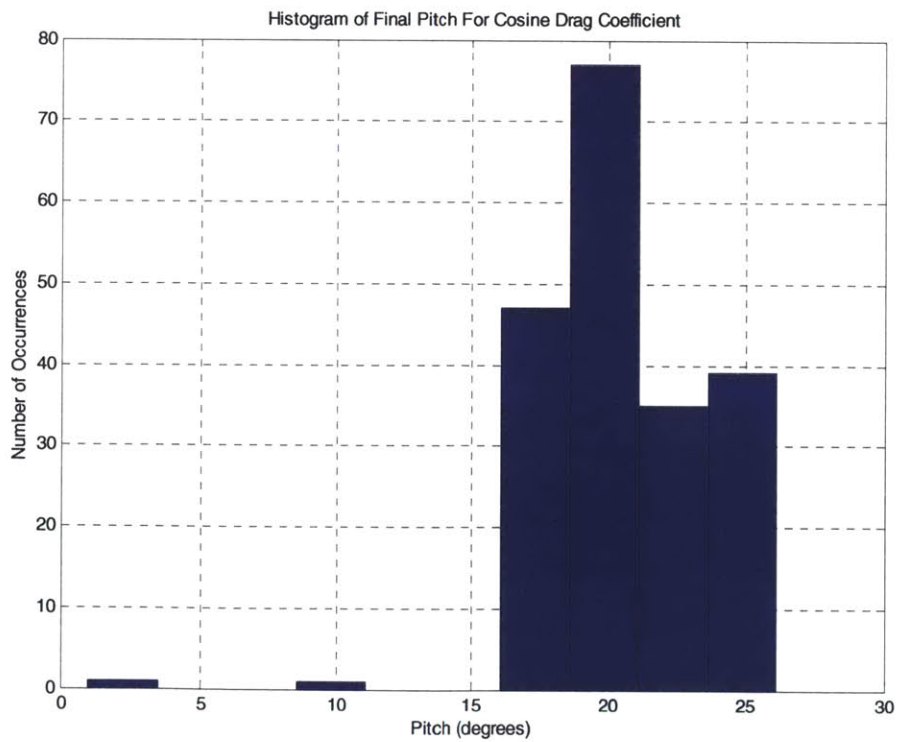


Figure 4.8 Bottom pitch angle histogram for cosine drag treatment for 200 simulations

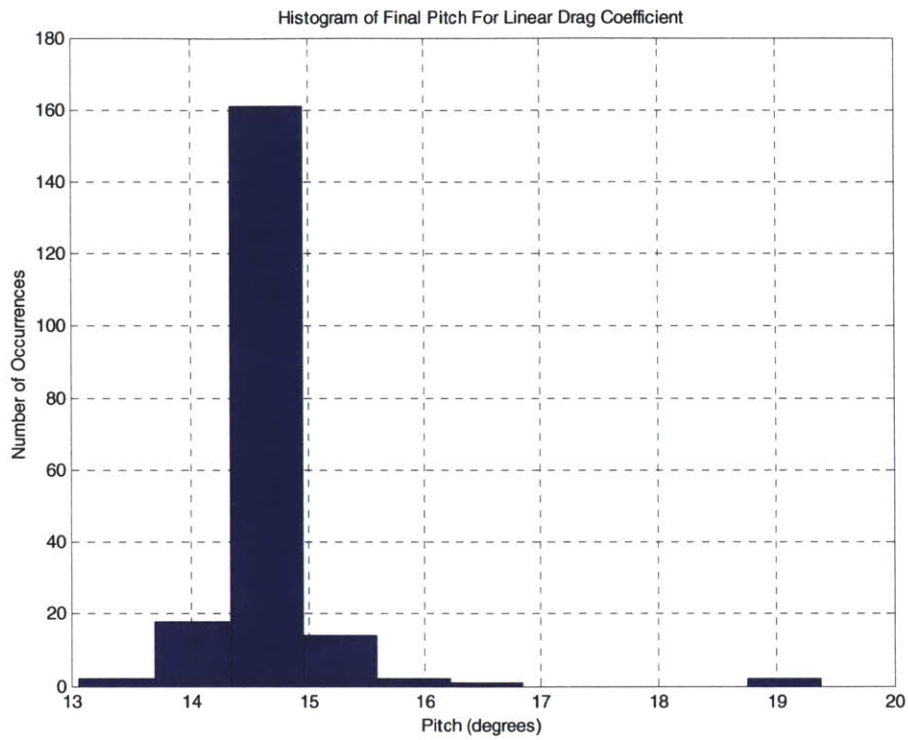


Figure 4.9 Bottom pitch angle histogram for linear drag treatment for 200 simulations

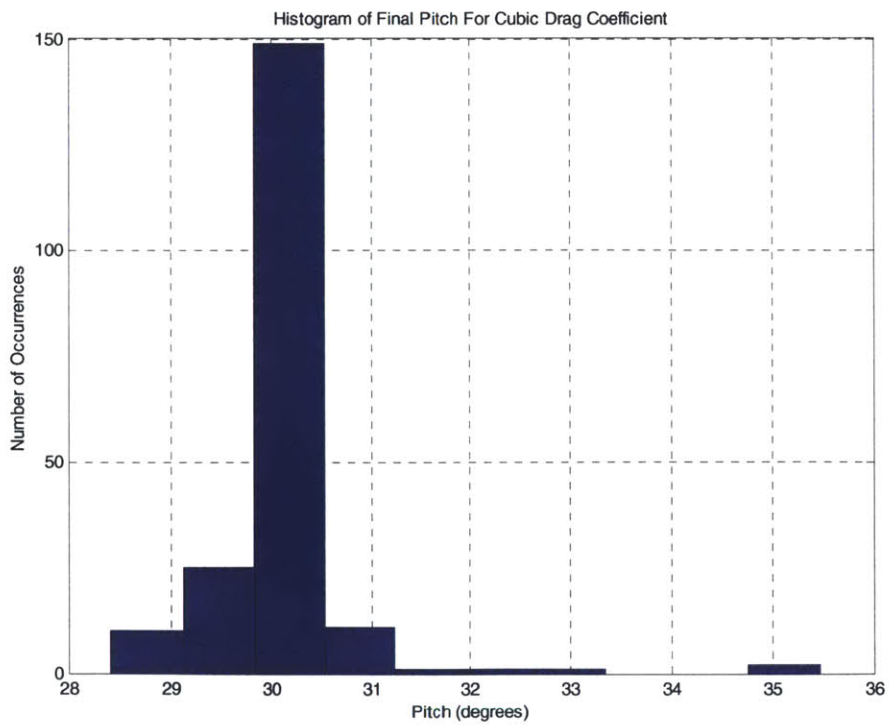


Figure 4.10 Bottom pitch angle histogram for cubic drag treatment for 200 simulations

Profile	Velocity Mean	Velocity STD	Pitch Mean	Pitch STD
Uniform	2.63	0.08	5.16	2.18
Cosine	3.54	0.16	20.51	3.01
Linear	3.74	0.064	14.70	0.57
Cubic	3.98	0.047	30.14	0.72

Table 4.1 Bottom velocity and bottom pitch angle means and standard deviations for different drag treatments.

4.2.2 Characterizations of Different Aspect Ratios

In addition to the type of profile used in the drag treatment, the aspect ratio (length to diameter) is an important parameter in determining the 3-D flow effects around the cylinder. As described in section 3.1.1, cylinders with aspect ratios greater than 15 exhibit drag characteristics similar to a 2-D model. Lower aspect ratios, between 6 and 15, show a decrease in overall drag with decreasing aspect ratios [30] while aspect ratios less than 6 do not continue to decrease the drag. Four values of the aspect ratio, 2.0, 4.5, 7.0 and 9.5 were examined with the same statistical input as shown in figures 4.1 and 4.2. Each aspect ratio was evaluated using the cosine drag profile as given by equation 3.1. The effect of the aspect ratio on the cosine distribution is shown in figure 4.11 against the normalized length of the cylinder. Mine dimensions were chosen such that the volume (and consequently, weight) of the mine remained constant for all the aspect ratios considered. Table 4.2 summarizes the basic mine physical parameters with further specifications in appendix D. In figures 4.12, 4.13, 4.14 and 4.15 a histogram of the bottom velocity is shown for each aspect ratio value. In figures 4.16, 4.17, 4.18 and 4.19 a histogram of the bottom pitch angle is shown for each aspect ratio. Table 4.3

summarizes the mean and standard deviation of the bottom velocity and pitch angle for each aspect ratio.

The model does reflect the trend that the lower the aspect ratio, the lower the overall drag as described by Zdravkovich [30]. As the aspect ratio increases, the mean bottom velocity decreases. This results from the strong three-dimensional flow lowering the overall drag on the cylinder. Another mechanism that would contribute to a lower bottom velocity would be the occurrence of see-saw motion. For a slender (high aspect ratio) mine released at an oblique angle, the onset of see-saw motion will slow the descent of the mine. Consequently, a low aspect ratio mine experiences higher bottom velocities more frequently because straight-slant motion is more likely to occur instead of see-saw motion. However, the slender mines are capable of achieving higher bottom velocities since a speed of 5 m/s was seen for the mine of aspect ratio 9.5. The high velocities for the more slender mines have the lowest occurrence as seen in figures 4.14 and 4.15 due to the dominance of see-saw motion.

A similar argument can be made for the bottom pitch angle. The less slender mines take a more horizontal attitude due to straight-slant motions occurring frequently. The more slender mines, experience a larger range of bottom angles as shown in figures 4.18 and 4.19 and in the variances listed in table 4.3. This variation in bottom pitch angle is a result of see-saw and travel motions. For a particular descent, the larger the release angle the more severe the oscillations of the see-saw motion. The bottom angle of 55 degrees shown in figure 4.17 is most likely a result of travel motion. For travel motion, the oblique release angle is maintained through the drop without oscillation. Travel motion is often the result when the center of mass is forward of the center of buoyancy or when the polynomial drag coefficient profile in equation 3.2 is used to model a release angle. Since symmetric drag profiles were used for the aspect ratio investigation and the center of mass coincided with the center of buoyancy, this travel motion was most likely induced by a large translational velocity. This serves to further illustrate that mine motions are complex and can result from additional mechanisms.

Aspect Ratio	Length (m)	Diameter (m)	Specific Weight	Nose	Volume (m ³)	Cg x (m)
2.0	1.4	0.674	1.9	N	0.535	0
4.5	2.4	0.533	1.9	N	0.535	0
7.0	3.22	0.460	1.9	N	0.535	0
9.5	3.81	0.423	1.9	N	0.535	0

Table 4.2 Mine properties for different aspect ratios. The mine dimensions were chosen that all mines being evaluated would have the same volume and weight

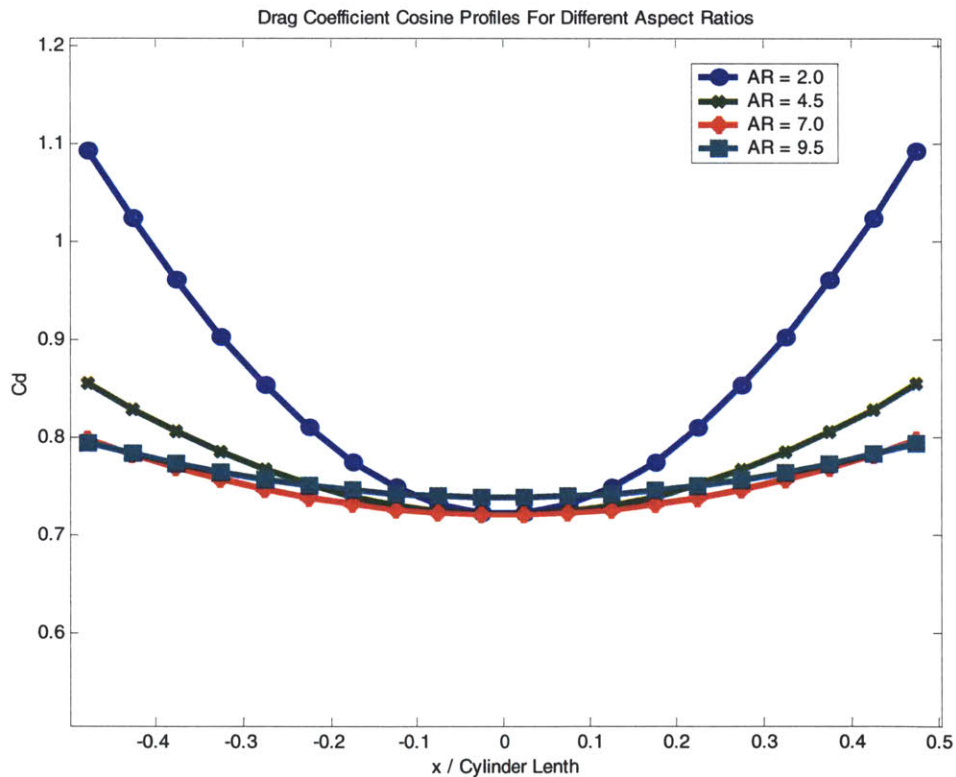


Figure 4.11 The drag coefficient profile over the normalized length of the cylinder as evaluated by equation 3.1 for different aspect ratios

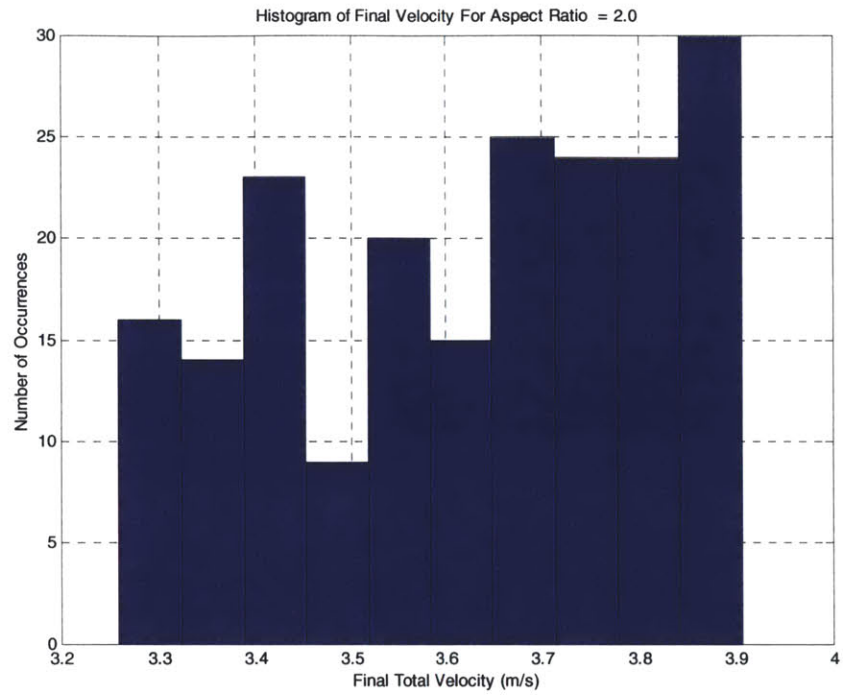


Figure 4.12 Bottom velocity histogram for aspect ratio of 2.0 for 200 simulations

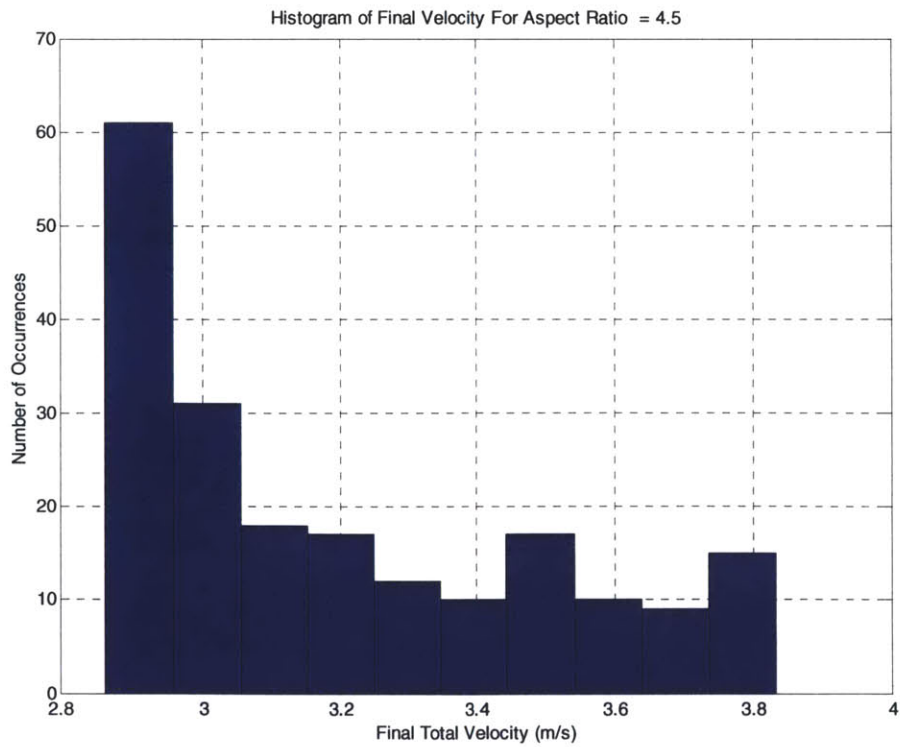


Figure 4.13 Bottom velocity histogram for aspect ratio of 4.5 for 200 simulations

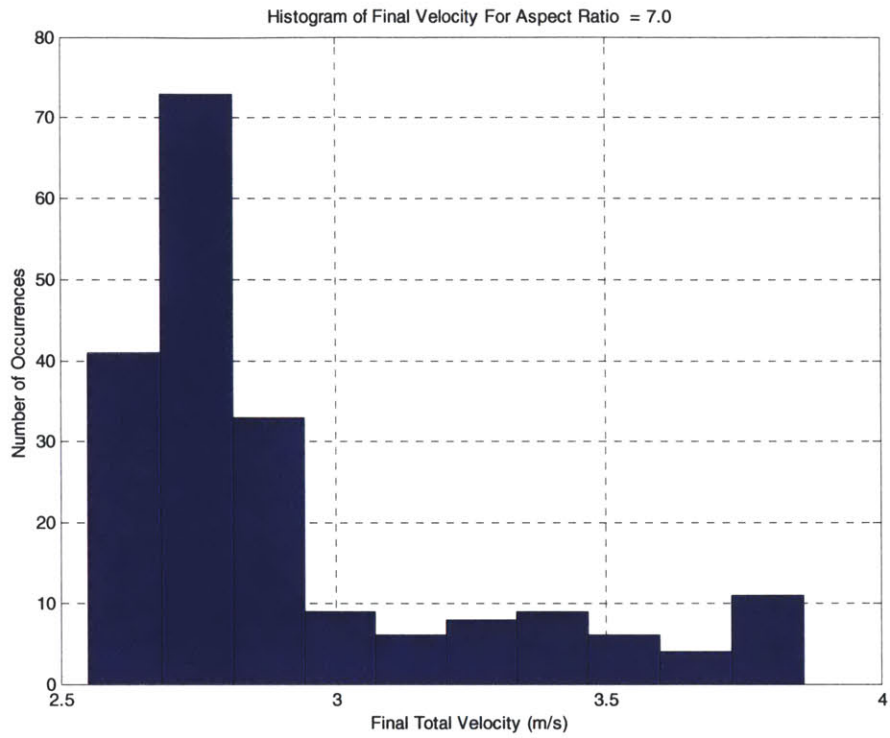


Figure 4.14 Bottom velocity histogram for aspect ratio of 7.0 for 200 simulations

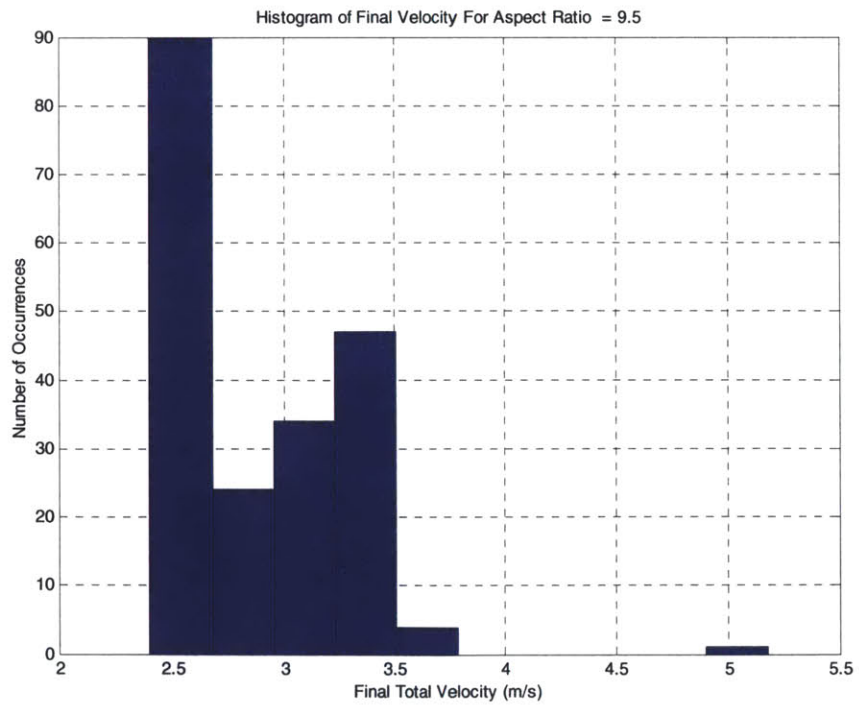


Figure 4.15 Bottom velocity histogram for aspect ratio of 9.5 for 200 simulations

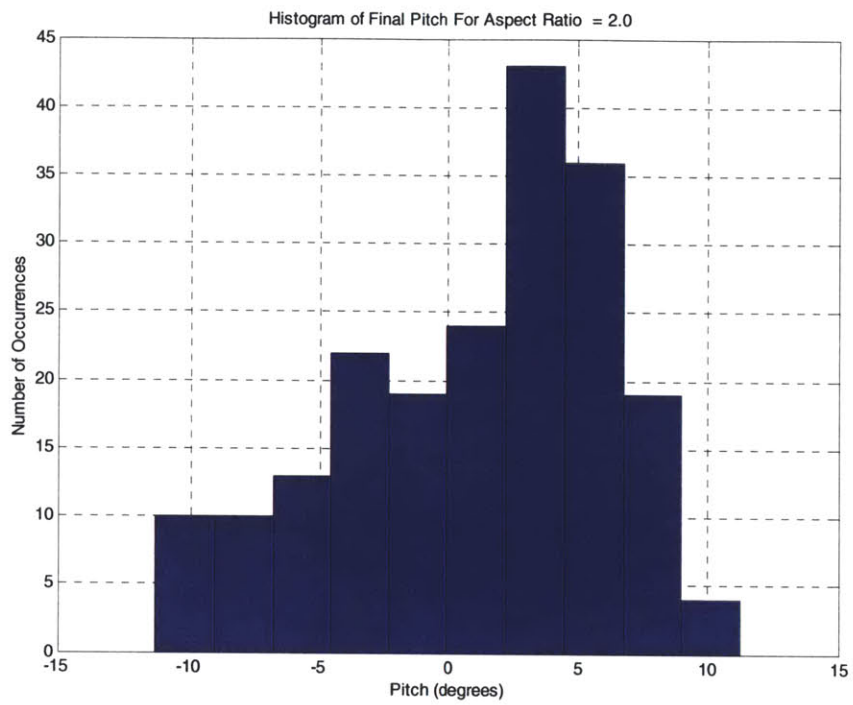


Figure 4.16 Bottom pitch angle histogram for aspect ratio of 2.0 for 200 simulations

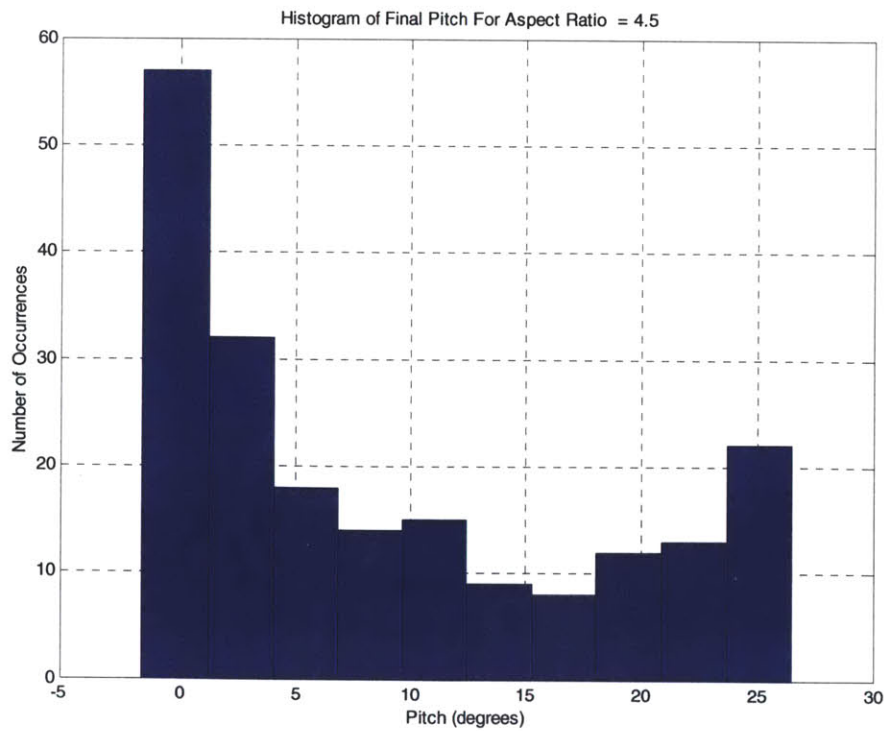


Figure 4.17 Bottom pitch angle histogram for aspect ratio of 4.5 for 200 simulations

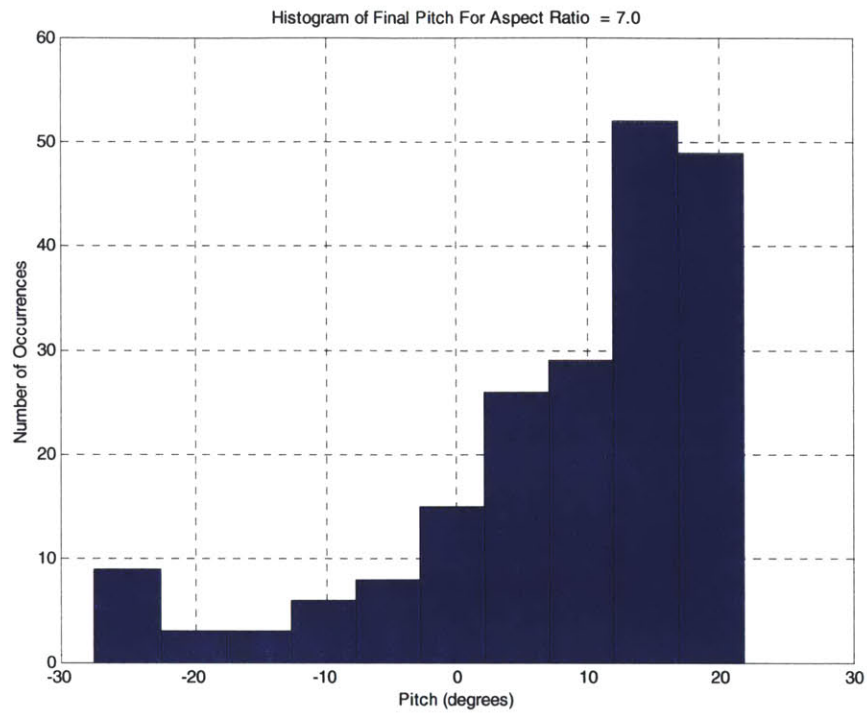


Figure 4.18 Bottom pitch angle histogram for aspect ratio of 7.0 for 200 simulations

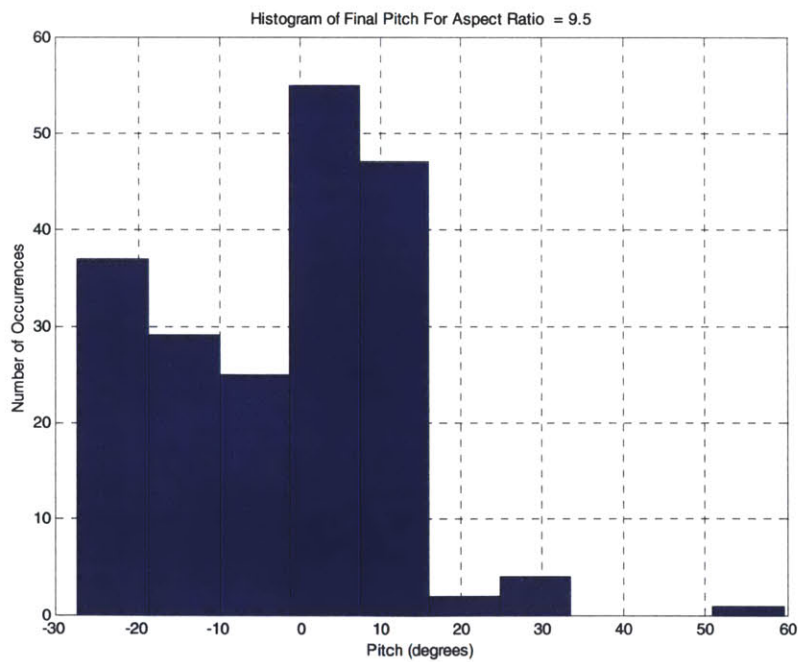


Figure 4.19 Bottom pitch angle histogram for aspect ratio of 9.5 for 200 simulations

Aspect Ratio	Velocity Mean	Velocity STD	Pitch Mean	Pitch STD
AR = 2.0	3.62003	0.18944	1.04038	5.15523
AR = 4.5	3.19478	0.29639	8.90366	9.31582
AR = 7.0	2.90789	0.33915	8.11744	11.56604
AR = 9.5	2.86151	0.43452	-3.02328	13.88066

Table 4.3 Bottom velocity and bottom pitch angle means and standard deviations for different aspect ratios.

4.3 Design Applications

The stochastic information generated from the Monte Carlo Simulation is also a powerful tool for design. Different cylindrical mines can be quickly evaluated to get a better understanding of how a prototype might fall through the water column. For example, consider a design parameter for a mine that requires the mine to have a similar percent of burial that is independent of release conditions for a given sediment bed. MINE6D could be used to provide the impact velocity and orientation needed to find the impact burial.

Mine Set	1	2	3	4	5
Density	1.8	1.8	1.9	1.9	2.0
Aspect Ratio	4.5	6.75	6.75	9.5	4.5
Cg x	0.1	0.1	0.1	0.2	0.25
Nose	Y	N	Y	Y	N

Table 4.4 Sample of Mine Characteristics Tested

Based on the “thumper” mine [21], a family of 20 mine designs were generated and divided up into 5 sets of mines. A sample of the characteristics used to generate these mines is shown in table 4.4 and the detailed characteristics of each of the 20 mines are listed in appendix C. These 20 mines were then tested using MINE6D over a wide range of initial conditions. The mean and standard deviations for the release conditions are also listed in appendix B. For this example, data and statistics were used to find the mine that had lowest variation in bottom velocity and orientation despite release conditions and environmental effects in the water column. Over 4,000 simulations were completed. Figure 4.16 shows the final velocity vs. initial pitch for 5 of 25 mines tested. From this plot, two types of mines, set 4 and set 5, have the small deviation from their mean bottom velocity. Figure 4.17 provides the bottom pitch angle for the tested mines. Set 5 has the smallest deviation from a mean final pitch angles. These statistics suggest that a mine of type 5 would be the best candidate to reproduce a similar impact velocity and orientation despite varying initial conditions and thus have a similar impact burial given the sediment composition. This type of simulation can be used in the design and optimization of mines.

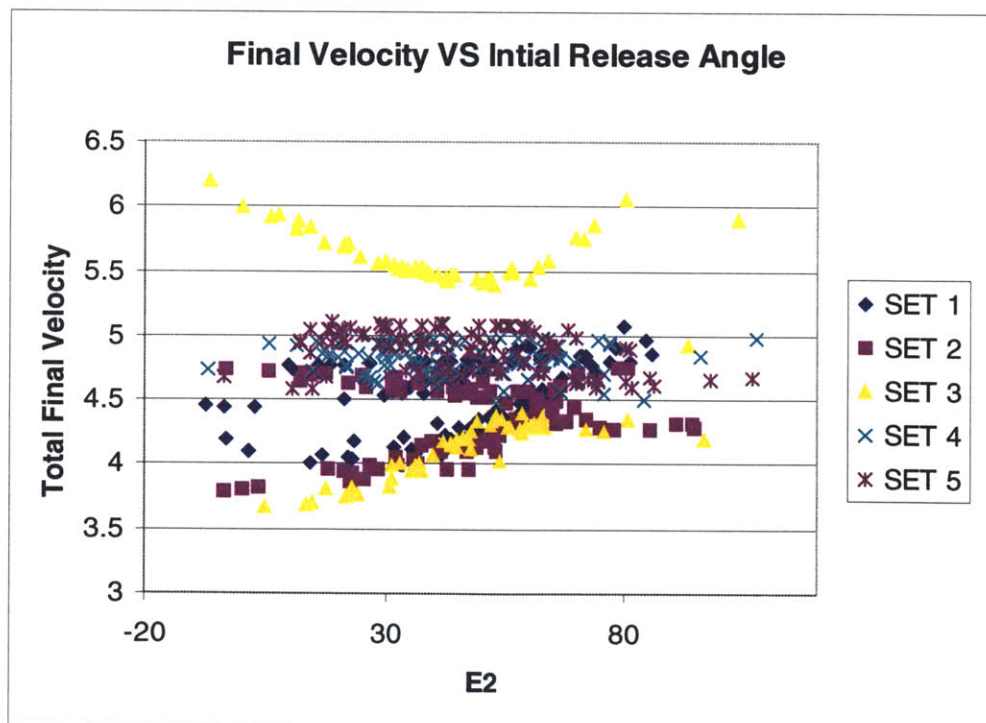


Figure 4.20 Plot of Final Velocity Vs Initial Release Angle For Sample Mine Types

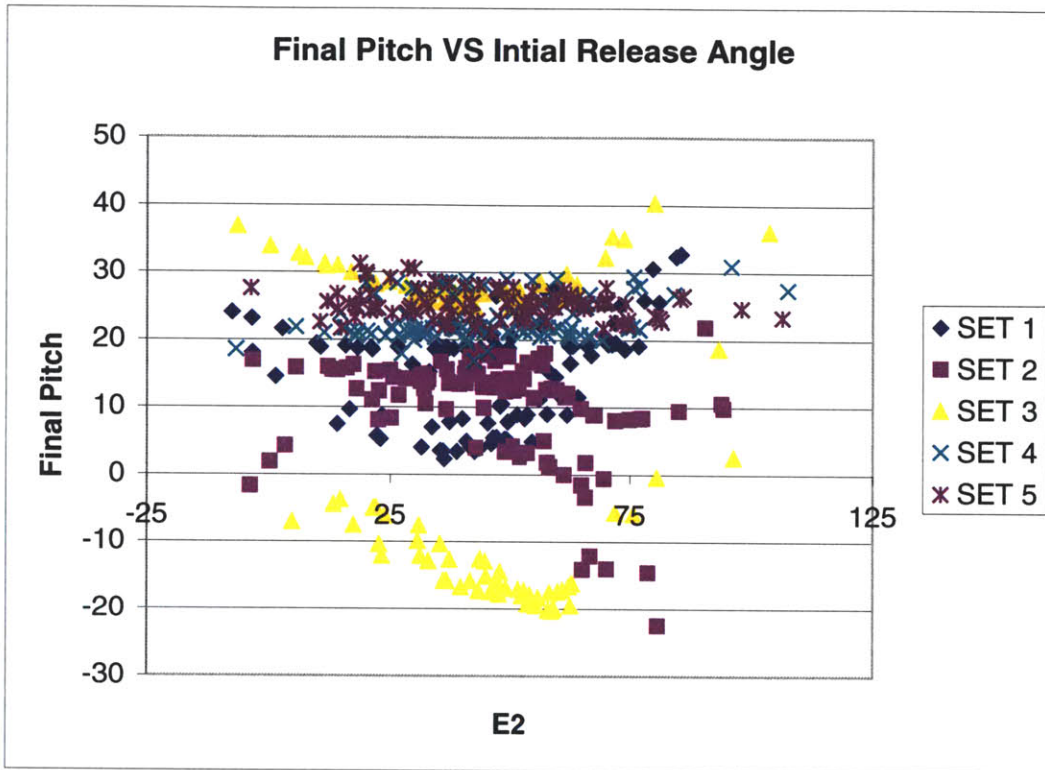


Figure 4.21 Plot of Final Pitch Vs Initial Release Angle For Sample Mine Types

Chapter 5

Conclusion

5.1 Summary

The developed deterministic model (MINE6D) advances the current mine burial prediction tools by reliably predicting the dynamics of mine drop motion near the sea bottom. This new six-degree of freedom physics based model includes physical effects due to water entry impact and air cavity formation, allows a sophisticated 3-D drag treatment, and accounts for the effect of environmental factors such as surface waves and variable currents. The deterministic model has been incorporated into a Monte Carlo Direct Simulation. The statistical information gathered from these simulations establishes stochastic transfer functions of the velocity and orientation of mines based on the mine's physical parameters and release conditions. The statistical information is also useful for the design of mines.

5.2 Future Work

Though the current model offers tremendous progress over previous tools, it still operates with limitations. Some of these limitations, such as using a quasi-steady drag treatment and the von Karman impact approximations, were employed to minimize computational cost. Other limitations could be improved by expanding the capabilities of the model. For example, currently only cylindrical mines are evaluated. In order to extend MINE6D to more general shapes, a thorough understanding of the drag of arbitrary geometries is needed.

The drag due to the air cavity is another area where further study is needed. The current model is restricted to very low Froude numbers. Though this model provides a reasonable approximation of the total cavity height, it does not capture the pinch off

location that would determine the size of the bubble that remains with the mine. Rewriting the equation 3.9 for z_c/H and h_c/H would produce the ratios of $1/3$ and $2/3$ respectively. However, experimental data collected for billiard balls shows that approximately $1/3$ of the cavity is below the pinch off point [25]. The movement of the free surface may contribute to the ratio of the bubble height to the total cavity height being smaller than expected. The mechanisms behind the shedding of the bubble as the mine continues downward also need further analysis. The decay rate from the shedding of bubbles for the current model was determined from five experimental horizontal drops of a full scaled mine [17]. However, this may not be appropriate for drops at oblique entry angles.

Bibliography

- [1] A.V. Abelev, P.J. Valent, N.G. Plant, and T.K. Holland “Evaluation and Quantification of Randomness in Free-fall Trajectories of Instrumented Cylinders.” in *Proceedings, Oceans 2003: Marine Technology and Ocean Science Conference*, San Diego, CA, 2003 September 22-26

- [2] John E. Williams and Steven R Vukelich, “The USAF stability and control digital datcom” Wright-Patterson Air Force Base, Ohio: Air Force Flight Dynamics Laboratory, Air Force Wright Aeronautical Laboratories, Air Force Systems Command, 1980

- [3] Garret Birkhoff and E.H. Zarantonello *Jets, Wakes, and Cavities*. New York: Academic Press, Inc, 1957 ch. 12, ch. 15.

- [4] S. Gaudet, “Numerical simulation of Circular Disks Entering the Free Surface of a fluid” *Physics of Fluids* vol. 10, no. 10, p. 2489, OCT 1998

- [5] David Gilbarg, and Robert A. Anderson, “Influence of Atmospheric Pressure on the Phenomena Accompanying the Entry of Sphere into Water”. *Journal of Applied Physics*, vol. 19, no. 2, Feb 1948

- [6] J.W. Glasheen and T.A. McMahon. “Vertical water entry of disks at low Froude numbers”. *Phys. Fluids*, vol 8 (8), p 2078, August 1996

- [7] Tsutomu Hayashi, Fumio Yoshino, Ryoji Waka, Seichi Tanabe, and Tetsuya Kawamura, “Turbulent Structure in a Vortex Wake shed from an Inclined Circular Cylinder”. *Journal of Japanese Society of Mechanical Engineers (JSME)*, no. 58, pg. 297, 1992

- [8] Tsutomu Hayashi, and Tetsuya Kawamura, "Non-uniformity in a flow around a yawed circular cylinder". *Flow Meas. Instrum*, vol. 6, no. 1, pp. 33-39, 1995
- [9] M. Lee, R.G. Longoria, and D.E. Wilson, "Cavity Dynamics in High Speed Water Entry", *Phys. Fluids*, vol 9 (3), March 1997
- [10] H.J. Lugt, "Autorotation". *Ann. Rev. Fluid Mechanics*, vol 15, pp. 123-147, 1983
- [11] S.C. Luo, "Flow past a finite length circular cylinder". in *Proceedings of the Third (1993) International Offshore and Polar Engineering Conference* June 6-11, vol. III p. 530, 1993
- [12] Albert May, "Vertical Entry of Missiles into Water". *Journal of Applied Physics*, vol 23, No. 12, Dec 1952.
- [13] Xiaoming Mei, Yuming Liu, and Dick K.P. Yue, "On the water impact of general two-dimensional sections." *Applied Ocean Research*, vol. 21, 1999
- [14] N. Metropolis, "The Beginning of the Monte Carlo Method." *Los Alamos Science*, no. 15, p. 125, 1987
- [15] H. Mutttery, "The Experimental Facts of Drag without Lift." *Handbuch der Experimentalphysik*, Berlin, vol. 4.2 521, 1932
- [16] S.E. Ramberg, "The effects of yaw and finite length upon the vortex wakes of stationary and vibrating circular cylinders". *J. Fluid Mech*, vol. 128, pp 81-107, 1983
- [17] M. Richardson, P. Valent, K. Briggs, J. Bradley, and S. Griffin, "NRL Mine Burial Experiments" in *Proceedings of the Second Australian-American Joint*

Conference on Technologies of Mine Countermeasures, Sydney, Australia, 27-29 March 2001.

- [18] Honh-Hui Shi, Motoyuki Itoh, Takuya Takami, "Optical Observation of the SuperCavitation induced by High-Speed Water Entry". *Journal of Fluids Engineerin*, vol. 122, Dec. 2000
- [19] A. Slaouti, & J.H. Gerrard, "An experimental investigation of the end effects on the wake of a circular cylinder towed through water at low Reynolds numbers". *Journal of Fluid Mechanics*, vol. 112, pp. 297-314, 1981.
- [20] P. Sulmont, and D.R. Rajaona, "Measurements of the Drag Forces on an Inclined Circular Cylinder in a Uniformly Accelerated and Decelerated Motion." *BOSS*, pp. 489-504, 1988
- [21] P.J. Valent & T.K. Holland, "Quick Look Report: Model mine hydrodynamic tests, NSW-Carderock." NRL Internal Memorandum (including movie files), 2001.
- [22] P.J. Valent, T.K. Holland, A.W. Green, S. Theophanis, S. King, M.D. Richardson, G.R. Bower, P. Congedo, and W. Lewis, "Observation of velocity and orientations of cylindrical bodies at terminal condition in water." in *Proc. 5th International Symposium on Technology and the Mine Problem*, Monterey, CA. 2002
- [23] M.M. Zdravkovich, V.P. Brand, G. Mathew and A. Weston, "Flow past short circular cylinders with two free ends", *J. Fluid Mech*, vol. 203, pp. 557-575, 1989
- [24] R. Zhao & O. M. Faltinsen, "Water Entry of Two-Dimensional Bodies", *Jour. Fluid Mechanics*, vol.246, 1993
- [25] Tadd Truscott & Jakob K Kominiarczuk, "Preliminary Cavity Experiments in the Impact Lab", MIT Internal Report, Nov 2004.

- [26] A. Dubi *Monte Carlo Applications in Systems Engineering*. West Sussex, England: Wiley, 2000, ch 3.
- [27] M Minnaert “On musical air bubbles and the sound of running water”, *Phil Mag* vol. 16, pp. 235-248, 1933
- [28] Yonghwan Kim, Y. Liu, D. KP Yue and P. Valent, “On the dynamics of a three-dimensional body falling through water”, *J. Fluid Mech*, submitted for publication.
- [29] R.A. Arnone and L.E. Bowen, “Prediction of the Time History Penetration of a Cylinder Through the Air-Water-Sediment Phases”. Naval Coastal Systems Center, Panama City, FL, Letter Report T34, 1980.
- [30] M. M. Zdravkovich, *Flow around circular cylinders : a comprehensive guide through flow phenomena, experiments, applications, mathematical models, and computer simulations*, Oxford, New York : Oxford University Press, 1997, vol. 2
- [31] W. Bolton, *Control Engineering*, Essex, England: Longman, 1998.

Appendix A : Sample Program Input

```

DATA FOR MINE6D-MC-VS1 - Thumper Mine
1.8 1025.0 9.806          ! BULK,DENSITY,GRAVI
2.4 0.533 15 5 8 1      ! CYLLEN,CYLDIA,NLENG,NC,ND,INOSE
0.7 1.0 0.5 0 0.0 1.0  ! CDR,CDXL,CDXR,ICD,CDEXTRA,FACTRAN
0.1 0.0 0.0            ! CGXYZ(I),I=1,3
100000. 0.0 0.0
0.00 0.3 0.0
0.00 0.0 0.3          ! (CI(I,J),J=1,3),I=1,3
0.0 0.0 0.0          ! VELOO(I),I=1,3
0.0 45.0 0.0         ! EULERO(I),I=1,3
0.0 0.0 0.0          ! OMEGALO(I),I=1,3
1 1 1 1 1 1          ! IDOF(I),I=1,6
0.01 10.1 40 1       ! DT,DEPTH,NBMODE, INDX_MOTOUT
1.0 0.25 5           ! VY_MEAN,VY_STD,NO_VY
45.0 20.0 5         ! EULER_MEAN,EULER_STD,NO_EULER
4                   ! NO_OBSERVE (MAXIMUM 5)
2.5 5.0 7.5 10.0    ! DEPTH_OBSERVE(I), I=1,NO_OBSERVE

```

Quantities of Interest:

BULK = Density Mine / Density Water

DENSITY = Density Water

GRAVI = Acceleration due to gravity

CYLLEN = Mine's Length

CYLDIA = Mine's Diameter

NLENG, NC, and ND correspond to number of body panels created

INOSE = 0 for blunt end, 1 for hemispherical end

CDR = drag coefficient at midsection

CDXL = drag coefficient in - x direction (for blunt end)

CDXR = drag coefficient in + x direction (for blunt or spherical end)

ICD = Drag Coefficient Profile Used: -1 for uniform, 0 for eqn 3.1, and N for eqn 3.2

CGXYZ = location of center of gravity for x, y, z

CI = coefficient of inertia matrix (3 x 3)

VELOO = initial velocity in x, y, z components

OMEGALO = initial angular rotation in x, y, z components

DT = Time Step Increment DEPTH = Water Depth

VY_MEAN = Mean of y velocity component

VY_STD = standard deviation of y velocity component

NO_VY = number of runs

EULER_MEAN = Mean of Euler angle from vertical

EULER_STD = standard deviation of Euler angle from vertical

NO_EULER = number of runs

Appendix B: Drag Treatment Detailed Mine Models

CI (for all Tests)	100000	0	0
	0	0.3	0
	0	0	0.3

Var Name	Test 18	Test 17	Test 5
Bulk	1.5	2.2	1.8
Density	1025	1025	1025
Gravity	9.806	9.806	9.806
CYLLEN	2.4	2.4	2.4
CLYDIA	0.533	0.533	0.533
NLENG	15	15	15
NC	5	5	5
ND	8	8	8
INOSE	1	0	1
CDR	0.72	0.72	1
CDXL	1	1	1
CDXR	0.5	1	0.5
ICD			
CDEXTRA	0	0	0
FACTRANS	2	1	1
CGX	0	0	0.25
CGY	0	0	0
CGZ	0.01	0	0.01
Vel X	0	0	0
Vel Y	0	0	1
Vel Z	-1	0	0
E 1	0	0	0
E 2	30	5	38
E 3	0	5	0
Omega 1	0	0	0
Omega 2	0	5	0
Omega 3	0	0	0
IDOF	6	6	6

Appendix C: Design Application Detailed Mine Models

Cl (for all Tests)	100000	0	0
	0	0.3	0
	0	0	0.3

Set 1 Contains: Mass 1 – Mass 4

Set 2 Contains: Mass 5 – Mass 8

Set 3 Contains: Mass 9 –Mass 12

Set 4 Contains: Mass 13 –Mass 16

Set 5 Contains: Mass 17 – Mass 20

File Name	MASS-1.DAT	MASS-2.DAT	MASS-3.DAT	MASS-4.DAT	MASS-5.DAT	MASS-6.DAT
Bulk	1.8	1.8	1.8	1.8	1.8	1.8
Density	1025	1025	1025	1025	1025	1025
Gravity	9.806	9.806	9.806	9.806	9.806	9.806
CYLLLEN	2.4	2.4	2.4	2.4	3.6	3.6
CLYDIA	0.5333	0.5333	0.5333	0.5333	0.5333	0.5333
NLENG	15	15	15	15	15	15
NC	5	5	5	5	5	5
ND	8	8	8	8	8	8
INOSE	1	1	1	1	0	0
CDR	0.7	0.7	0.7	0.7	0.7	0.7
CDXL	1	1	1	1	1	1
CDXR	0.5	0.5	0.5	0.5	0.5	0.5
ICD	0	3	0	3	0	3
CDEXTRA	0	0	0	0	0	0
FACTTRANS	1	1	1	1	1	1
CGX	0.1	0.1	0.1	0.1	0.1	0.1
CGY	0	0	0	0	0	0
CGZ	0	0	0	0	0	0
Vel X	0	0	0	0	0	0
Vel Y Mean	1	1	1	1	1	1
Vel Y STD	0.25	0.25	0.25	0.25	0.25	0.25
No. of Runs	10	10	10	10	10	10
Vel Z	0	-1	-2	-3	0	-1
E 1	0	0	0	0	0	0
E 2 Mean	45	45	45	45	45	45
E 2 STD	20	20	20	20	20	20
No. of Runs	20	20	20	20	20	20
E 3	0	0	0	0	0	0
Omega 1	0	0	0	0	0	0
Omega 2	0	0	0	0	0	0
Omega 3	0	0	0	0	0	0
IDOF	6	6	6	6	6	6

File Name	MASS-7.DAT	MASS-8.DAT	MASS-9.DAT	MASS-10.DAT	MASS-11.DAT	MASS-12.DAT
Bulk	1.8	1.8	1.9	1.9	1.9	1.9
Density	1025	1025	1025	1025	1025	1025
Gravity	9.806	9.806	9.806	9.806	9.806	9.806
CYLLEN	3.6	3.6	3.6	3.6	3.6	3.6
CLYDIA	0.5333	0.5333	0.5333	0.5333	0.5333	0.5333
NLENG	15	15	15	15	15	15
NC	5	5	5	5	5	5
ND	8	8	8	8	8	8
INOSE	0	0	1	1	1	1
CDR	0.7	0.7	0.7	0.7	0.7	0.7
CDXL	1	1	1	1	1	1
CDXR	0.5	0.5	0.5	0.5	0.5	0.5
ICD	0	3	0	3	0	3
CDEXTRA	0	0	0	0	0	0
FACTTRANS	1	1	1	1	1	1
CGX	0.1	0.1	0.1	0.1	0.1	0.1
CGY	0	0	0	0	0	0
CGZ	0	0	0	0	0	0
Vel X	0	0	0	0	0	0
Vel Y Mean	1	1	1	1	1	1
Vel Y STD	0.25	0.25	0.25	0.25	0.25	0.25
No. of Runs	10	10	10	10	10	10
Vel Z	-2	-3	0	-1	-2	-3
E 1	0	0	0	0	0	0
E 2 Mean	45	45	45	45	45	45
E 2 STD	20	20	20	20	20	20
No. of Runs	20	20	20	20	20	20
E 3	0	0	0	0	0	0
Omega 1	0	0	0	0	0	0
Omega 2	0	0	0	0	0	0
Omega 3	0	0	0	0	0	0
IDOF	6	6	6	6	6	6

File Name	MASS-13.DAT	MASS-14.DAT	MASS-15.DAT	MASS-16.DAT	MASS-17.DAT
Bulk	1.9	1.9	1.9	1.9	2.0
Density	1025	1025	1025	1025	1025
Gravity	9.806	9.806	9.806	9.806	9.806
CYLLEN	5.1	5.1	5.1	5.1	2.4
CLYDIA	0.5333	0.5333	0.5333	0.5333	0.5333
NLENG	15	15	15	15	15
NC	5	5	5	5	5
ND	8	8	8	8	8
INOSE	1	1	1	0	0
CDR	0.7	0.7	0.7	0.7	0.7
CDXL	1	1	1	1	1
CDXR	0.5	0.5	0.5	0.5	0.5
ICD	0	3	0	3	0
CDEXTRA	0	0	0	0	0
FACTRANS	1	1	1	1	1
CGX	0.2	0.2	0.2	0.2	0.25
CGY	0	0	0	0	0
CGZ	0	0	0	0	0
Vel X	0	0	0	0	0
Vel Y Mean	1	1	1	1	1
Vel Y STD	0.25	0.25	0.25	0.25	0.25
No. of Runs	10	10	10	10	10
Vel Z	0	-1	-2	-3	0
E 1	0	0	0	0	0
E 2 Mean	45	45	45	45	45
E 2 STD	20	20	20	20	20
No. of Runs	20	20	20	20	20
E 3	0	0	0	0	0
Omega 1	0	0	0	0	0
Omega 2	0	0	0	0	0
Omega 3	0	0	0	0	0
IDOF	6	6	6	6	6

File Name	MASS-18.DAT	MASS-19.DAT	MASS-20.DAT
Bulk	2.0	2.0	2.0
Density	1025	1025	1025
Gravity	9.806	9.806	9.806
CYLLEN	2.4	2.4	2.4
CLYDIA	0.5333	0.5333	0.5333
NLENG	15	15	15
NC	5	5	5
ND	8	8	8
INOSE	0	0	0
CDR	0.7	0.7	0.7
CDXL	1	1	1
CDXR	0.5	0.5	0.5
ICD	3	0	3
CDEXTRA	0	0	0
FACTRANS	1	1	1
CGX	0.25	0.25	0.25
CGY	0	0	0
CGZ	0	0	0
Vel X	0	0	0
Vel Y Mean	1	1	1
Vel Y STD	0.25	0.25	0.25
No. of Runs	10	10	10
Vel Z	-1	-2	-3
E 1	0	0	0
E 2 Mean	45	45	45
E 2 STD	20	20	20
No. of Runs	20	20	20
E 3	0	0	0
Omega 1	0	0	0
Omega 2	0	0	0
Omega 3	0	0	0
IDOF	6	6	6

Appendix D: Aspect Ratio Detailed Mine Models

Var Name	AR 2.0	AR 4.5	AR 7.0	AR 9.5
Bulk	1.9	1.9	1.9	1.9
Density	1025	1025	1025	1025
Gravity	9.806	9.806	9.806	9.806
CYLLEN	1.4	2.4	3.22	3.810
CLYDIA	0.674	0.533	0.460	0.423
NLENG	15	15	15	12
NC	5	5	5	5
ND	8	8	8	8
INOSE	0	0	0	0
CDR	0.72	0.72	0.72	0.72
CDXL	1	1	1	1
CDXR	1	1	1	1
ICD	0	0	0	0
CDEXTRA	0	0	0	0
FACTRANS	1	1	1	1
CGX	0	0	0	0
CGY	0	0	0	0
CGZ	0	0	0	0
Vel X	0	0	0	0
Vel Y Mean	1	1	1	1
Vel Y STD	0.25	0.25	0.25	0.25
No. of Runs	10	10	10	10
Vel Z	-1	-1	-1	-1
E 1	0	0	0	0
E 2 Mean	45	45	45	45
E 2 STD	20	20	20	20
No. of Runs	20	20	20	20
E 3	0	0	0	0
Omega 1	0	0	0	0
Omega 2	0	0	0	0
Omega 3	0	0	0	0
IDOF	6	6	6	6